AD-A241 123

6-499-AN-01 (1)

DEFORMATION, FRACTURE AND EXPLOSIVE PROPERTIES OF REACTIVE MATERIALS

Principal Investigator: Dr. J.E. Field

EUROPEAN RESEARCH OFFICE

United States Army
London W1, England

Contract No. DAJA45-90-C-0023

ANNUAL REPORT JUNE 1991

Physics & Chemistry of Solids
Cavendish Laboratory
University of Cambridge
Madingley Road
Cambridge CB3 OHE
England

91-11653

"The research supported in this document has been made possible through the support and sponsorship of the US Government through its European Research Office of the US Army. This report is intended only for the internal management use of the Contractor and the US Government"

91 9 26 073

SECURITY CLASSIFICATION OF THIS PAGE

REPORT DOCUMENTATION PAGE

Form Approved OMB No. 0704-0188

1a. REPORT SECURITY CLASSIFICATION Unclassified	1b RESTRICTIVE MARKINGS
2a. SECURITY CLASSIFICATION AUTHORITY	3. DISTRIBUTION/AVAILABILITY OF REPORT Approved for public release; distribution unlimited.
2b. DECLASSIFICATION/DOWNGRADING SCHEDULE	
4. PERFORMING ORGANIZATION REPORT NUMBER(S)	5. MONITORING ORGANIZATION REPORT NUMBER(S) R&D 4380A-R-AN
6a. NAME OF PERFORMING ORGANIZATION University of Cambridge 6b. OFFICE SYMBOL (*If applicable*)	7a. NAME OF MONITORING ORGANIZATION USARDSG (UK)
6c. ADDRESS (*City, State, and ZIP Code*) Cavendish Laboratory Madingley Road, Cambridge, CB3 OHE, UK	7b. ADDRESS (*City, State, and ZIP Code*) P O Box 65 FPO New York 09510 - 1500
8a. NAME OF FUNDING/SPONSORING ORGANIZATION USARDSG(UK) 8b. OFFICE SYMBOL (*If applicable*) AMXSN-UK-RA	9 PROCUREMENT INSTRUMENT IDENTIFICATION NUMBER DAJA45 90-C-0023
8c. ADDRESS (*City, State, and ZIP Code*) P O Box 65 FPO New York 09510-1500	10. SOURCE OF FUNDING NUMBERS PROGRAM ELEMENT NO. / PROJECT NO. / TASK NO / WORK UNIT ACCESSION NO
11. TITLE (*Include Security Classification*) Deformation, Fracture and Explosive Properties of Reactive Materials.	
12. PERSONAL AUTHOR(S) Dr J E Field, Dr N K Bourne, Dr J M Huntley Dr S M Walley and S J P Palmer	
13a. TYPE OF REPORT Annual 13b. TIME COVERED FROM May 90 TO May 91	14 DATE OF REPORT (*Year, Month, Day*) 1991 June 30 15. PAGE COUNT 50
16 SUPPLEMENTARY NOTATION	
17. COSATI CODES FIELD / GROUP / SUB-GROUP	18 SUBJECT TERMS (*Continue on reverse if necessary and identify by block number*) Explosives, ignition, impact, sensitiveness, hot spots, high speed photography, deformation, fracture, PETN, PBXs propellants.

19. ABSTRACT (*Continue on reverse if necessary and identify by block number*)

See overleaf

20. DISTRIBUTION/AVAILABILITY OF ABSTRACT ☒ UNCLASSIFIED/UNLIMITED ☐ SAME AS RPT ☐ DTIC USERS	21. ABSTRACT SECURITY CLASSIFICATION Unclassified
22a. NAME OF RESPONSIBLE INDIVIDUAL Dr R E Reichenbach	22b TELEPHONE (*Include Area Code*) 01-409-4423 22c OFFICE SYMBOL AMXSN-UK-RA

DD Form 1473, JUN 86 *Previous editions are obsolete.* SECURITY CLASSIFICATION OF THIS PAGE

impact tests using

ABSTRACT

A range of techniques has been developed for studies of the behaviour of explosives when impacted and for recording their strength. failure and ignition properties. They include a drop-weight facility with transparent anvils, an instrumented drop-weight machine, a miniaturised Hopkinson bar system for high rate of strain property measurement, laser speckle for studies of deformation and fracture of PBX's, an automated system for analysing speckle and moiré records, and a heat sensitive film technique for recording the position and temperatures of hot spots. The report describes (section 2) the use of the transparent anvil drop-weight apparatus for various studies of impacts on propellant grains, including 'normal' and low vulnerability propellants. Section 3 discusses the latest developments and recent applications with our laser speckle and moiré research. We now have the ability to combine these high spatial resolution techniques with high speed photographic recording. Impact on 2-D composite disc samples (section 3.3) shows the importance of 'liner' materials in reducing impact stresses. Section 4 describes the application of laser speckle photography to measure the in-plane displacement fields resulting from the compression loading of cylindrical grains of inert solid gun propellant. Microstructural studies on the failure surfaces of PBX's are presented in section 5. Finally section 6 gives results on a photographic study of shock-induced cavity collapse of both inert gels and reactive materials. Shock pressures were in the range up to 8GPa.

are presented.

propellants for guns is discussed.

DTIC
COPY
INSPECTED
8

A-1

1. INTRODUCTION

As described in previous reports (see for example reports of 1988 and 1989) a range of techniques have been developed in this laboratory for studies of the behaviour of explosives when impacted and for recording their strength, failure, and ignition properties. They include (i) a drop-weight facility with transparent anvils; this allows observation of the sample by high-speed photography throughout the impact event (ii) an instrumented drop-weight machine which is used for the determination of H50's and stress/strain behaviour at strain rates in the range 102 to 103 s^{-1} (iii) a direct impact Hopkinson bar of 10mm diameter to cover the strain rate range 102 to 2×103 s^{-1}. It is mounted vertically which makes the positioning of the sample particularly easy, (iv) a miniaturised direct impact Hopkinson bar system for high rate of strain property measurement for the range 104 to 105 s^{-1}, (v) a Brazilian test apparatus which can stress disc samples of PBX's to failure at low strain rates, (vi) laser speckle and moiré techniques for studies of deformation and fracture. The speckle technique is routinely used with the Brazilian test geometry for deformation studies of PBX's. Automated techniques have been specially developed for analysing the speckle and moiré records. These have been significantly speeded up during the present grant period. The optical techniques have wide application to a range of impact and fracture situations and various studies on both explosive and inert materials are now in progress, (vii) a heat sensitive film technique for recording the position and temperature of 'hot spots'.

Section 2 describes the use of the transparent drop-weight facility for two studies on propellant grains. In the first, particular geometric arrangements were studied to evaluate the importance of trapped gas heating on the ignition process. In the second, discs cut from propellant grains with a hexagonal array of holes were impacted: a normal and a low vulnerability propellant were studied.

Section 3 discusses the latest developments and recent applications with our laser speckle and moiré photography research. The speckle techniques are now routinely used to study the deformation and failure properties of PBX's over a wide range of strain rates. A particularly interesting development (section 3.3) has been the ability to record and follow deformation and fracture events at microsecond interframe intervals. High resolution moiré photography has been used (section 3.4) to study the impact of rectangular projectiles on composite disc specimens: the discs can be regarded as 2-D sections through simulated artillery shells. The experiments demonstrate the substantial reductions in strains which can be achieved through the use of liners.

Section 4 describes the application of laser speckle photography to measure the in-plane displacement fields resulting from the compressive loading of cylindrical grains of inert solid gun propellant. The experimental approach is shown to be a viable one and in future research we plan to use a larger Instron testing machine which will achieve higher loads.

Section 5 describes our latest research on the microstructure of PBX's particularly after they have been strained to failure.

Finally section 6 presents results of a photographic study of the shock-induced collapse of 2-D arrays of cavities. Shock pressures ranged from 0.3 to 8 GPa and the cavity arrays were in (i) inert gels and (ii) reactive emulsions.

2. DROP-WEIGHT IMPACT STUDIES ON PROPELLANTS

2.1 Arrays of propellant grains

The sensitivity to impact of five different compositions of propellant grains in 3×3 close-packed arrays was tested using the drop-weight apparatus shown schematically in figure 1. It was originally developed by Blackwood & Bowden (1952) and has more recently been extensively employed by Heavens, Field, Swallowe and others in the study of the sensitivity to impact of a wide range of energetic materials (see the references by Heavens & Field (1974), Swallowe & Field (1981), Field, Swallowe & Heavens (1982), Krishna Mohan & Field (1984), Krishna Mohan *et al.* (1984), and Field *et al.* (1985)). High-speed photography shows that the arrays coalesce into more-or-less circular discs (figures 2, 3). Three of the propellant grain compositions tested deflagrated, and the deflagration usually started from a corner of the array (figure 3). This led to the suggestion that deflagration was caused by the collapse of the gas space trapped between the grains at the corner. To test this hypothesis, 'cross-shaped' arrays of the three compositions that ignited were tested. These cross shapes consisted of a 'head' of four grains arranged in a square with a tail of three further

grains leading off from one corner (figures 4, 5). Deflagration was observed always to start from the head of the cross, confirming that it was the enclosed air space that was sensitizing the grains.

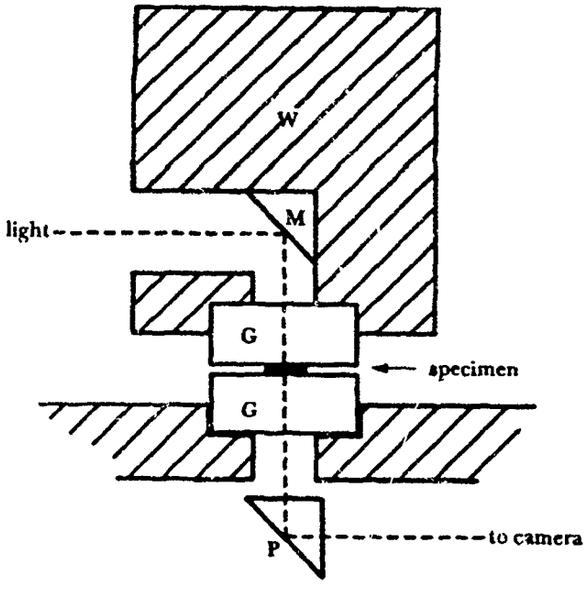

Fig. 1 Schematic diagram of the dropweight apparatus modified for high-speed photography. W, weight; M, mirror; G, glass anvils; P, prism.

2.2 Statistics

When performing experiments with high-speed photography, usually only one or two drops are carried out until a successful sequence is obtained. Therefore further drops must be carried out to obtain statistics on the sensitivity of propellants tested under these conditions. So extra drops were performed on the 3×3 arrays. Three of the compositions deflagrated every drop and one never deflagrated (see Table 1).

TABLE 1

Statistics on 3×3 arrays of homogeneous propellant grains

Composition	Number of drops	Number of deflagrations
P1	5	5
P3	5	5
P4	5	2 (1 very strong)
P5	5	5 (all very violent)
P6	5	0

Note: the composition designations given in this table refer to the grains used in the cast compositions (see December 1989 report).

2.3 Discs cut from propellant formed into slotted tubes

Two sorts of propellant were tested in the apparatus of figure 1. The first (propellant 1) was a conventional charge; the second was an experimental low vulnerability charge. Both had a hexagonal array of burning holes (see figures 6, 8, 10, 11, 12). The conventional charge deflagrated strongly in both drops presented here (figures 6, 8). As a disc 2mm thick, deflagration was associated with only one of the holes, but as a disc 0.5mm thick, deflagration can clearly be seen initiating and propagating from several of the burning holes. The low vulnerability composition did not deflagrate when in the

form of discs 2mm thick or greater (see figures 10, 11 and Table 2). But when tested in the form of discs less than 2mm thick approximately half the drops (out of seven) yielded a deflagration event (see figures 12, 13 and Table 2).

TABLE 2

Statistics on discs of low vulnerability propellant cut from slotted tube

Disc thickness/mm	Number of drops	Number of deflagrations
< 2	7	3
≥ 2	6	0

3. Laser Speckle and Moiré Photography: Recent Developments and Applications

3.1. Introduction

Optical strain measurement techniques have a number of advantages over conventional strain gauges. They provide wholefield, rather than pointwise, information, and can be non-contacting, which is a significant benefit with low modulus materials like polymer bonded explosives (PBXs). Reinforcement effects associated with strain gauges are eliminated.

Research has been carried out on two optical techniques over the past year: laser speckle photography and high resolution moiré photography. Laser speckle photography is the simplest technique, but involves substantial analysis of the photographs to extract the displacement and strain fields. An image processing system was built seven years ago, and fringe analysis techniques developed, to automate the analysis procedure. A review was given in section 5.2 of the previous final report (December 1989). The technique is now used routinely, in conjunction with the Brazilian test, for strength and strain-to-failure measurements on PBXs. Speckle photography was used for the strain measurements on the propellant grains supplied by Dr Robert Lieb (section 3.2). Two further developments are described in this section: a new fringe analysis algorithm based on maximum likelihood estimation, which results in random errors up to 6 times lower than obtainable with Fourier transform analysis; and a pulsed laser/ high speed camera system for measuring dynamic strain fields by speckle photography.

The second technique, high resolution moiré photography, has also recently been developed for dynamic strain measurements. Further developments have been made since the last final report: the use of reflective phase gratings means that the technique is now applicable to opaque materials; and a telecentric imaging system eliminates errors due to out-of-plane motion of the specimen. Experiments have been carried out on simulated artillery shells.

A new image processing system is being constructed, suitable for digital speckle and moiré interferometry. This should allow strain-fields to be measured in real-time, without the development of film and separate analysis stage required by speckle photography.

3.2. Maximum likelihood analysis of speckle photographs

Laser speckle photography involves illuminating the specimen with a laser beam, and recording two images on film: one before, the other after the deformation. Light is scattered from the surface features of the specimen to create a fine random speckle pattern in the image plane. Movement of the specimen causes a corresponding motion of the speckles; the developed film therefore consists of many speckle pairs. The in-plane displacement vector of any point on the specimen surface can be obtained by measuring the speckle displacement at the corresponding point on the film. This is normally done by probing the photograph with a narrow laser beam. A diffraction pattern is formed which is similar to a that from a mask containing two small apertures, and is therefore commonly called the "Young's fringes" pattern. The displacement vector at the point being probed can be deduced from the spacing and angle of the Young's fringes. Complete analysis of a speckle photograph may involve several hundred fringe patterns, which is why we have developed automated fringe analysis techniques. A comparison of four algorithms was made in Huntley (1989), in which it was found that the method based on Fourier transformation of the fringe pattern gave the lowest random errors. Fourier analysis does not, however, take account of the multiplicative nature of the speckle noise in the Young's fringes. The fringe minima have a lower noise level than the fringe maxima, so that the Fourier transform (which treats all datapoints with equal weight) can in principle

be improved upon in this application. Appendix 1 describes a method based on maximum likelihood analysis, which incorporates knowledge of the probability density function for speckle noise. The random errors are reduced by up to a factor of 6 compared to the Fourier transform method. The computation time is currently about 100 times longer than that required by the Fourier transform, but the recent availability of low-cost high performance workstations means that the algorithm could become applicable on a routine basis.

3.3. High speed laser speckle photography

Laser speckle photography can in principle be used to measure dynamic displacement fields, but a high-power laser is required. A pulsed ruby laser, with Glan-air polariser and Pockels cell inside the cavity, has been multiply Q-switched and used as a light-source for recording high speed speckle photographs (Huntley *et al.* 1990). Each Q-switched pulse is about 50-100 ns long, and the main technical difficulty is synchronising these pulses with the individual frames of the rotating mirror high speed camera. This is a particular concern in the case of speckle photography, since decorrelation of the two speckle patterns at a given frame will occur if the mirror is not in the same position for the first and second exposures. The timing precision required to prevent significant decorrelation is about 5% of the interframe time. To achieve this precision, a photodetector is placed at each of the relay lenses, with a small flashlamp at the corresponding point of the main objective lens. Each photodetector therefore produces a signal when the mirror is in the correct position to expose that frame. The output of a logical OR operation on the photodetectors is then amplified and used to drive the Pockels cell. Further details are given in Appendix 1.

Tests have so far been carried out with interframe times in the range 2-8 μs. In general, the energy per pulse is most uniform at high interframe times, and the fluctuations can be reduced by increasing the pump rate, and decreasing the time the Q-switch is kept open. The energy per pulse (10-20 mJ) is sufficient to expose Agfa 10E75 holographic emulsion at a magnification of 1:1. Double exposure photographs have been recorded by running the camera twice, and translating the specimen between runs. Good Young's fringes were obtained at interframe times down to 2 μs, indicating that speckle decorrelation is not a problem; an example is shown in Fig. 10 of Appendix 1. The (image plane) speckle dimensions are 6 and 26 μm in the horizontal and vertical dimensions: this variation in sensitivity is a consequence of the rectangular aperture in the high speed camera. The horizontal dimension corresponds to a spatial frequency of 160 lines mm^{-1}, which is four times the claimed resolution of the camera. When analysed by the Fourier transform method of fringe analysis, the random errors in the horizontal and vertical displacement components are approximately 0.2 and 1.1 μm, respectively.

The camera and laser system is currently being used for dynamic measurements of the strain field due to ball impact on PBXs. Experiments to measure the dynamic fracture toughness of PBXs are also planned.

3.4. High resolution moiré photography: disc impact

Moiré photography involves superimposing two gratings: one is attached to the specimen, the other acts as a reference. Beating between the two gratings results in a fringe pattern, which represents a contour map of the in-plane displacement component perpendicular to the reference grating lines. The contour interval equals the pitch of the specimen grating, so the sensitivity is improved as the grating is made finer. In the last final report, and in Huntley & Field (1989), a high resolution moiré technique was described in which the specimen grating is imaged onto the reference grating with a specially modified lens. The lens modifications allow good contrast fringe patterns to be recorded at a grating frequency of 150 lines mm^{-1}, which is about four times the maximum normally feasible with conventional moiré photography.

The technique has since been further developed in two significant ways: (1) the use of reflective phase gratings means that it is now applicable to opaque materials, and (2) the optical arrangement is now telecentric so that out-of-plane displacements cause no fringe shifts and hence no errors in the in-plane strains. The improvements are described in detail in Appendix 2. In brief, the technique consists of applying a reflection phase grating of 75 lines mm^{-1} in a thin layer of either epoxy resin or silicone rubber to the specimen surface. Silicone rubber has a low modulus compared to most PBXs, so the technique could in principle be used for dynamic strain measurements on PBXs. The specimen grating is imaged onto the reference grating by the modified camera lens, which selects just the +1

and -1 diffraction orders from the specimen grating, doubling its effective frequency to 150 lines mm^{-1}.

Experiments have been carried out to investigate the effect of impact by rectangular projectiles on composite disc specimens. The discs can be regarded as 2-D sections through simulated artillery shells. The discs are 5 mm thick and consist of a central polycarbonate region with a diameter of 15.9 mm, 19.1 mm, or 22.2 mm, surrounded by a copper ring of external diameter 25.4 mm and wall thickness 1.6 mm. The intervening region was filled with silicone rubber. Epoxy reflection gratings were applied to the polycarbonate region, and the aim was to measure the level of strains that were present in the polycarbonate region for different thicknesses of rubber. Phosphor bronze projectiles were fired by means of a rectangular bore gas gun, giving projectile velocities of 56.0 ± 1.1 m s^{-1}. Three high speed sequences, corresponding to rubber thicknesses of 0, 1.55 and 3.15 mm, are shown in Figs. 14, 15 and 16. Impact occurred horizontally from the left; the gratings were vertical so the fringes represent the horizontal displacement component, and compressive strains show up as a decrease in the fringe spacing. With a specimen grating frequency of 150 lines mm^{-1}, the sensitivity is 6.7 μm $fringe^{-1}$.Only the central polycarbonate region is visible. The interframe time is 5 μs. In Fig. 14 (rubber thickness = 0 mm), the strains are very high and the dark region near the point of impact is a Schlieren effect where the diffracted beams from the specimen grating are deflected by surface tilt away from the slots in the lens. This is not a significant problem in Figs. 15 or 16. In Fig. 15 (rubber thickness = 1.55 mm), a compressive stress wave can be seen entering the polycarbonate from the left, crossing the disc in approximately 15 μs. This reflects from the right hand surface as a tensile wave, cancelling the effect of the incident wave as can be seen in frame 3. Figure 15 was analysed by the Fourier transform method (Huntley & Field 1989), and the displacement field measured from the eight frames is shown in Fig. 17, where the contour interval is 2 μm. In Fig. 16 (rubber thickness = 1.55 mm), the compressive strains are much lower: in frame 2, for example, the maximum occurs close to the impact point, and is under 1 millistrain. These experiments therefore demonstrate the substantial reduction in strains which can be achieved through the use of a liner. The technique is currently being used to investigate the displacement field around cracks in polymers under stress wave loading.

3.5. Image processing equipment

A new image processing system is currently being constructed for digital speckle pattern interferometry, comprising a Sun 386i workstation, Digital Imaging Systems framestore (DIS3000), and EEV photon camera. The combination of camera and framestore allows clocking of the CCD data, pixel by pixel, directly into the framestore memory, thereby eliminating pixel jitter which can cause noise in a speckle interferometry experiment. The framestore, camera and computer have been delivered, and are now working well. Preliminary speckle interferometry experiments have been carried out using a diode laser; phase stepping was achieved by altering the laser injection current, which changes the wavelength slightly.

A fibre optic delivery system has been designed to provide specimen illumination for digital speckle and moiré interferometry experiments. Light from a HeNe laser will be passed through a 50:50 beamsplitter and into two single mode polarisation preserving fibres. The output end of each fibre will be mounted at the focal point of a gimbal-mounted camera lens, to provide a versatile dual collimated beam illumination system. Phase stepping will be achieved by incorporating a piezoelectric translator into one arm of the interferometer. The optical fibres (with integral launching lenses) have been delivered. and work satisfactorily.

4. Deformation of Propellent Grains

4.1 Introduction

Laser speckle photography has been used to investigate the in-plane displacement fields resulting from the compressive loading of a cylindrical grain of inert solid gun propellent, between flat brass anvils.

4.2 Experimental

The details of the recording and analysis of laser speckle patterns have been fully described in previous reports.

An inert sample of a solid gun propellent, was placed between two flat brass anvils with its circular face containing a hexagonal array of burn holes lying in the plane of the anvils. The specimen was loaded in compression by moving the top anvil at a constant rate of 50 μm per minute, up to a maximum load of 40 kg. The specimen image was magnified by 5.19 times by the recording lens, so that one quadrant of the circular face adjacent to the moving anvil, filled a frame of film.A series of seven double-exposure speckle patterns were recorded during loading of the sample.at F2.8 using a He-Ne laser. Individual double-exposure speckle patterns were obtained using an exposure time of 2s with an inter-exposure time of 40s. The exposure time was selected to give an adequate exposure whilst ensuring that the movement of the speckle pattern on the film was less than the smallest speckle that could be resolved by the recording lens. Failure to satisfy this requirement results in blurring of the speckle pattern. The smallest speckle that can be recorded using illumination from a He-Ne laser, at F2.8 and a magnification of 5.19 times, is 2.6 μm.This determines the sensitivity of the technique, in that in-plane displacements smaller than this can not be measured.with the existing analysis system.

The in-plane displacements were determined by probing the double-exposure speckle patterns with an unexpanded laser beam from a He-Ne laser, and analysing the Young's fringe patterns obtained, on an image processing system described in previous reports. Each pattern was analysed on a square grid of 27 by 27 points with a separation of 0.7mm. This corresponds to a spatial resolution on the specimen surface of 0.135 mm. The time taken to analyse a single fringe pattern is typically 10s, consequently it takes approximately two hours to analyse a complete speckle pattern.

4.3 Results

Contour plots showing the in-plane displacement components U_x and U_y, parallel to the horizontal and vertical axes, are shown in figures 18 to 20., corresponding to loads of 22.9, 30.5 and 39.1 kg respectively. These plots were obtained by adding the displacements from individual specklegrams starting at frame 1 up to and including frame 7. A small correction factor was included in the calibration factor to allow for displacements occurring during the period when the film in the camera was advanced to new frame by the motor drive.

During the initial loading of the sample, in frames 1 and 2, a small in-plane rotation occurred. The presence of this rotation shows up in the contour plots. In the case of a pure in-plane rotation alone, the U_x and U_y contours will consist of equally spaced horizontal and vertical parallel lines respectively, in which the spacing is inversely proportional to the magnitude of the rotation. In this case the magnitude of the rotation was calculated to be 1.8 milliradians.

In addition to in-plane rotation there is also a rigid-body translation present. Its presence is manifested by the large values of the displacement components as shown in the contour plots. The largest translations occur in the negative Y direction, i.e. the loading direction. By the end of frame 7 this was calculated to be 64 μm, compared with about 10 μm in the negative X direction for the horizontal translation. It should be noted that in trying to estimate the in-plane translations, the displacement due to any in-plane rotation is first subtracted from the data on the assumption that rotation is centred on the axis of symmetry. Should this not be this case. then the subtraction will introduce a small rigid-body translation into the data.

The contour plots corresponding to loads of 30.5 and 39.1 kg, start to show evidence of strains developing in the grain. This is most clearly seen underneath the loading anvil, close to the axis of symmetry, (X=0.25, Y= 2.75) in the U_y contour plots. The compressive strains at this point have been estimated to be 1.2 and 2.0 millistrain respectively, compared with tensile strains of 0.3 and 0.9 millistrain. Also the U_x contour plot corresponding to frame 7, suggests that there is the start of some strain concentration in the region between the burn holes, (i.e. X= 1.0, Y= 1.5) at this load.

4.4 Discussion

The in-plane displacements due to the deformation of the propellent grain up to a load of 40 kg are quite small when the rigid-body motions are subtracted, i.e. typically several μm. These displacements are comparable with the size of the smallest speckle that could be resolved by the recording lens. In the absence of the rigid-body displacements, the deformation could not have been detected. For this reason calculation of the in-plane strain fields is unreliable. It was not possible with the existing apparatus, to apply significantly higher loads. However, the results are encouraging and confirm the usefulness of the technique. It is planned to repeat these experiments on an Instron testing machine, in which substantially higher loads can be used and the consequent deformation of

the grain can be more accurately determined, thereby enabling the strain fields to be more reliably ascertained.

5. MICROSTRUCTURE OF PBX'S

5.1 Introduction

The fracture of a TATB and HMX based PBX, containing Kel-F800 and HTPB (Hydroxy-terminated-Polybutadiene) polymer binders respectively, have been studied using scanning electron microscopy, and polishing techniques. Samples of the different compositions were fractured in the Brazilian test.

5.2 Experimental

The TATB based composition consists of 85/15/5 wt% TATB/HMX/KEL-F800. Samples were supplied by AWE Aldermaston, in the form of discs 10.23mm in diameter by 2.50 mm thick. The tensile strength was measured by means of the Brazilian test, whilst laser speckle photography was used to measure the failure strain. This composition failed in a brittle manner, with an audible click. The fracture surfaces could be exposed by gently flexing the broken sample between the fingers. The fracture surfaces were then mounted side by side on an SEM microscope stub, and sputtered with gold for examination in the Cambridge Stereoscan S250. A low accelerating voltage of 5.1 kV was used in order not to burn or decompose the specimen.

The HMX based composition consists of 95/5 wt% HMX/HTPB, again in the form of discs with the above dimensions. The fracture of the HMX/HTPB composition could not be investigated using this technique as the material fails in a rather ductile manner, and the additional damage caused by physically pulling the fracture surfaces apart cannot be discriminated from the original fracture. In this case a sample of the composition was polished, etched and the binder stained prior to testing it in the Brazilian test.

The sample was polished using a 2 μm Cerirouge powder and etched with Iso-Butyl-Methyl-Ketone, followed by washing with distilled water. The Polyurethane binder was stained black, by exposing the polished sample to ruthenium tetroxide vapour for several hours in a sealed container.

5.3 Results

Figure 21 shows a fractured crystal probably of TATB. The surface steps suggest a cleavage fracture of the crystal. The top half of the crystal is missing, and appears to have left behind an impression in the polymer, which suggests that fracture occurred after fabrication. This may have happened during the Brazilian test although it is not possible to be certain. The micrograph also shows areas where it appears that crystals have been pulled out of the polymer matrix, leaving behind empty impressions.

Figure 22 was recorded at the same magnification. The main feature of interest is the twinned crystal on top of which is lying a layer of polymer. The exposed polymer appears to have resulted from the debonding of an adjacent crystal. The thickness of the polymer layer is of the order of 1 μm. Part of the crystal has fractured parallel to a twin plane, leaving behind an impression of its original shape

Figure 23 shows two examples of fractured crystals. In both cases part of the crystal is missing leaving behind a hole. In the lower of the two micrographs there is a fractured layer of the Kel-F binder on the right hand side of the crystal, with an approximate thickness of 3 μm.

Figure 24 shows an example of a large fractured crystal of approximately 60 μm in the top micrograph. The lower micrograph shows a crystal which has partially debonded from the matrix. The angular faces of the large crystal have very small discrete particles of polymer adhering to their surface. This suggests that when debonding occurs, the polymer remains essentially intact leaving behind a comparatively clean crystal surface.

Figure 25 shows essentially the same features as before, in that the crystals appear to debond cleanly from the matrix.

Figure 26 shows a montage of the fracture route through the HMX/HTBP composition after being fractured in the Brazilian test. The montage shows that there is a predominance of interfacial failure between the crystals and binder. In particular this appears to occur at the sites of the larger crystals. Crystal fracture appears to be relatively rare, and tends to occur when the a crystal impedes the propagation of a crack.

5.4 Discussion

The SEM micrographs of the Kel-F based composition show that both crystal fracture and debonding occur. The holes associated with some of the fractured crystals, may suggest that they fractured first and that the fracture halves subsequently became separated, leaving behind an impression of their original size and shape. It is possible that at the comparatively high stresses at which this material fractures (typically 3 to 4 MPa) the crystals may be fracturing under this stress. The Kel-F 800 binder is a stiff polymer, and as such appears in cases of debonding to detach itself cleanly from the explosive crystals.

The composition containing the HTPB binder fails at a much lower tensile stress than the composition containing the Kel-F binder, i.e. typically at 1.8 MPa compared with about 3.5 MPa. Fracture of the HMX crystals at this stress is unlikely. Interfacial failure appears to be the main cause of failure, especially at the sites of large crystals.

6. Cavity Collapse and Explosive Initiation

A two-dimensional technique is used to study the features of shock-induced cavity collapse which give rise to the initiation of an emulsion explosive. The cavities (of sizes varying between 5 and 12 mm) are punched out of either a thin sheet of gelatine or of an emulsion explosive. The sheet is then clamped between polymethylmethacrylate (PMMA) blocks. In some experiments it is sandwiched between two other pieces of gelatine and placed into a water-filled aquarium. The sheets are photographed as the cavities are collapsed using a high-speed image convertor camera framing at up to 5×10^6 frames per second (fps) and schlieren optics are used to visualise shocks. The shocks are introduced either by the impact of a flier plate or by using an explosive plane-wave generator (PWG). This gives a range of shock pressures from ca. 0.3 to 8 GPa. When a single cavity is collapsed in gelatine by shocks travelling at close to acoustic velocities, an asymmetrical closure is observed. The upstream wall is spalled across the cavity by the incident shock forming a high-speed jet which crosses the cavity and impacts the downstream wall. High pressure is induced in the liquid at this point and a shock is transmitted into the surrounding fluid. The gas within the cavity is rapidly compressed and heated, and luminescence can be observed in the final stages of collapse. The jet penetrates the downstream wall and a pair of linear vortices is formed which convects downstream in the flow. When shock pressures increase the jet velocity is elevated so that it may exceed the shock velocity within the medium. When a cavity is collapsed in a sodium nitrate/ammonium nitrate emulsion explosive, several regions of ignition are observed. Reaction starts in the vapour within the cavity and in the material around the heated gas pockets during the final stages of closure. Later there is ignition of the material at the point of jet impact. The latter was found to be the principal ignition mechanism. When an array of cavities is created within an emulsion, a collapse wave drives the cavity closure and an associated inhomogeneous ignition front travels with it.

Figure 27 (a) shows three frames taken from a sequence in which a 12 mm cavity containing air is collapsed by a 0.26 GPa shock. The exposure time for each frame is ca. 0.5 μs. A gelatine sheet is clamped between PMMA blocks and the shock is introduced by flier-plate impact. In frame 1 the incident shock, S, can be seen entering the sequence from below. The schlieren is adjusted to reveal density variations in the air within the cavity. The initial dappled appearance of the air is due to a low amplitude compression wave travelling ahead of the main shock and induced by the blast of air expelled from the gun barrel ahead of the flier-plate. An air shock, A, can be seen travelling away from the downstream wall at the acoustic velocity for air. Frame 2, taken 60 μs after frame 1, is representative of an intermediate stage of the collapse. The air shock has reflected from the downstream wall, returned, reflected from the involuted upstream wall and now travels back across the cavity. The upstream wall has deformed to form a jet which crosses the cavity at constant velocity. The intricate shape of the air shock is a consequence of the temporal variations in its confinement. Frame 3 shows the final stages of collapse and was taken 110 μs after frame 1. The jet has impacted the downstream wall sending out a shock wave into the surrounding fluid. Two lobes of compressed gas are trapped in the closure. As a consequence of jet penetration of the downstream wall, a pair of linear vortices subsequently forms which convects downstream in the following flow.

Figure 28(b) shows a single frame from a sequence of two 6 mm cavities collapsing in an aquarium. The exposure time of the frame is ca. 20 ns. The collapse is caused by a 1.88 GPa shock from a PWG. A schematic diagram is placed next to the sequence showing the position of the two cavities relative to the shock and relevant features of the collapse. Due to the lateral extent of the

shock wave when viewed from the side, its slight curvature masks details of the collapse behind the shock front. The left hand cavity is in the process of collapse and a liquid jet can be seen crossing the cavity. An estimate of the jet velocity (measured from other frames in the sequence) is 5 km s^{-1}. This indicates that at elevated pressures jet velocities can exceed collapsing-shock velocities. Since a further shock is transmitted into the undisturbed region at the jet tip, this can be regarded as a mechanism by which signals can be propagated ahead of the incident shock. A second cavity on the right-hand side of the frame is in the final stages of collapse. Two flashes of light, L, are visible correlating in position with the trapped lobes of gas discussed in relation to the acoustic regime collapse of figure 27 (a). The light emission is believed to result from the luminescence of gas heated by adiabatic compression during the collapse.

The sequence of figure 27 (a) is typical of collapses observed when the incident shocks are close to acoustic. The principal features of such collapses are:–

(i) formation of a jet travelling perpendicular to the shock front,
(ii) a constant velocity jet,
(iii) shock transmission into the surrounding fluid on jet impact,
(iv) production of isolated lobes of trapped gas after jet penetration of the downstream wall,
(v) formation of linear vortices convecting in the flow after the shock wave has passed.

At higher shock pressures the basic features of collapse behaviour are preserved. However, three variations are worthy of note. Firstly, the jet no longer travels at constant velocity. Secondly, its velocity can exceed that of the collapsing shock. Thirdly, the gas can be sufficiently compressed that temperatures can rise sufficiently to allow gas-luminescence. A more detailed account of the collapse behaviour of single cavities at varying pressures can be found elsewhere (Bourne and Field 1991).

Figure 28 shows the collapse of a 3×3 square array of 5 mm cavities punched into the emulsion. The shock, S, enters from below and is of the same pressure as before. Again the emulsion is sandwiched between PMMA blocks and spacers confine the emulsion at the sides. The interframe time is 2 μs and the exposure time for each frame is 0.1 μs. The shock, S, can be seen entering frame 1 below. The cavity on the right of the first row shows two points of light, R, at the shock front. These are believed to be two reacting sites produced at irregularities on the cavity wall. A double image of these sites is apparent, due to refraction through shocks running at different velocities in the PMMA confinement and the emulsion. The material ahead of the point of jet impact reacts in frame 2 and the sites persist until frame 6. They are characteristically kidney-shaped. Again a double images occur. The second row is nearing the end of collapse in frame 5. Reaction is beginning first in the central of the three cavities due to the slight curvature of the shock front. In the next frame the sites grow in the central and the right-hand cavities.

The collapse of cavity arrays was studied by Dear and Field (1988). They showed that a collapse wave is formed which travels through an array. Bourne and Field (1990) considered the velocity of such a wave and found it to be dependent upon the shock pressure, the cavity diameter and inter-cavity spacing. Only the first row of a square array is collapsed by the incident shock. The second row being collapsed by the rebound shock caused by jet impact. Thus collapse proceeds in a row by row manner as observed in the sequence and the reaction sites are found in the material ahead of the downstream cavity wall. Also, since jet velocity can exceed the shock velocity the reaction initiates ahead of the incident shock. The reacting region ignites at the point of jet impact but a propagating deflagration wave is not produced. The lifetime of the sites is at maximum 7 μs and on average 5 μs. The sequence presents a macroscopic picture of the heterogeneous reaction zone in a shocked explosive.

REFERENCES

Blackwood J.D. & Bowden F.P. (1952) "The initiation, burning and thermal decomposition of gunpowder" *Proc. Roy, Soc. Lond.* A **213** 285

Bourne N.K., and Field J.E., (1990) "Collapsing cavities in reactive and non-reactive media" in preprints of the 19th international conference on high-speed photography and photonics, Cambridge, September, 1991.

Bourne N.K., & Field J.E., (1991) "Shock induced collapse of single cavities in liquids" *J. Fluid Mech.* (submitted).

Dear J.P., and Field J.E., (1988) "A study of the collapse of arrays of cavities" *J. Fluid Mech.* **190**, 409-425.

Field J.E., Palmer S.J.P., Pope P.H., Sundarajan R. & and Swallowe G.M. (1985) "Mechanical properties of PBX's and their behaviour during drop-weight impact" in *Proc. 8th Int. Symp. on Detonation,* Albuquerque. U.S.A.

Field J.E., Swallowe G.M. & Heavens S.N. (1982) "Ignition mechanisms of explosives during mechanical deformation" *Proc. Roy. Soc. Lond.* A **382** 231

Heavens S.N. & Field J.E. (1974) "The ignition of a thin layer of explosive by impact" *Proc. Roy. Soc. Lond.* A **338** 77

Huntley J.M. (1989), "Speckle photography fringe analysis: assessment of current algorithms", *Appl. Opt.* **28** 4316-22 .

Huntley J.M. and Field J.E., (1989) "High resolution moiré photography: application to dynamic stress analysis", *Opt. Eng.* **28** 926-933 .

Huntley J.M., Whitworth M.B., Palmer S.J.P., Goldrein H.T., and Field J.E., (1990) "Automatic speckle photography fringe analysis: application to electron microscopy and high speed photography", *Proc. Intl. Conf. Hologram Interferometry and Speckle Metrology*, Baltimore, U.S.A., 5-8 November, 337-342.

Krishna Mohan V. & Field J.E. (1984) "Impact initiation of hexanitrostilbene" *Combustion and Flame* **56** 269

Krishna Mohan V, Field J.E. & Swallowe G.M. (1984) "Effects of physical inhomogeneities on the impact sensitivity of solid explosives: A high-speed photographic study" *Combustion Sci. and Tech.* **44** 269

Swallowe G.M. & Field J.E.(1982) "The ignition of a thin layer of explosive by impact: The effect of polymer particles" *Proc. Roy. Soc. Lond.* A **379** 389

FIGURES

Figure 20. Contour plots showing the in-plane displacement components U_x and U_y parallel to the X and Y axis respectively at a load of 31.9 kg.

Figure 21. SEM micrographs of the cleavage fracture of a crystal, showing surface steps on the fracture surface.

Figure 22. SEM micrographs showing a twinned crystal, probably of TATB,underneath a layer of polymer. Also note the impressions left behind by debonded crystals.

Figure 23. SEM micrographs showing two examples of fractured crystals. In both cases part of the crystal is missing, leaving behind a hole.

Figure 24. SEM micrographs showing a large 60 μm fractured crystal in the top micrograph. The lower micrograph shows a partially debonded crystal, with small particles of binder adhering to the angular faces.

Figure 25. SEM micrographs showing partially debonded crystals.

Figure 26. Montage showing the fracture route through a sample of HMX/HTPB, fractured in the Brazilian test after polishing and staining. Note the interfacial failure at the sites of the large crystals.

Figure 27. The asymmetrical collapse of cylindrical, air filled bubbles in gelatine. (a). The incident shock, S, of pressure 0.26 GPa, collapses a 12 mm cavity. Note the air shock, A, bouncing within the cavity and the formation of a jet which impacts in frame 3 isolating two lobes of trapped gas. (b) the shock, of strength 1.88 GPa, collapses a 6 mm cavity. The jet is crossing the left-hand cavity faster than the incident shock is moving. A second cavity on the right has already collapsed and two points of light are seen from the trapped lobes of luminescing gas.

Figure 28. The collapse of a 3×3 square array of 5 mm cavities punched into the emulsion. The shock, S, enters from below causing two points of reaction, R, on the upstream wall. A double image occurs here and with other reaction sites because of refraction through the shock in the confining blocks. Collapse of the array proceeds row by row with reaction sites ahead of the incident shock. The average lifetime of sites is 5 μs. The sequence is unlit.

APPENDICES

1. **Automatic speckle photography fringe analysis: Application to electron microscopy and high speed photography.**

2. **High speed photography of high resolution moiré patterns.**

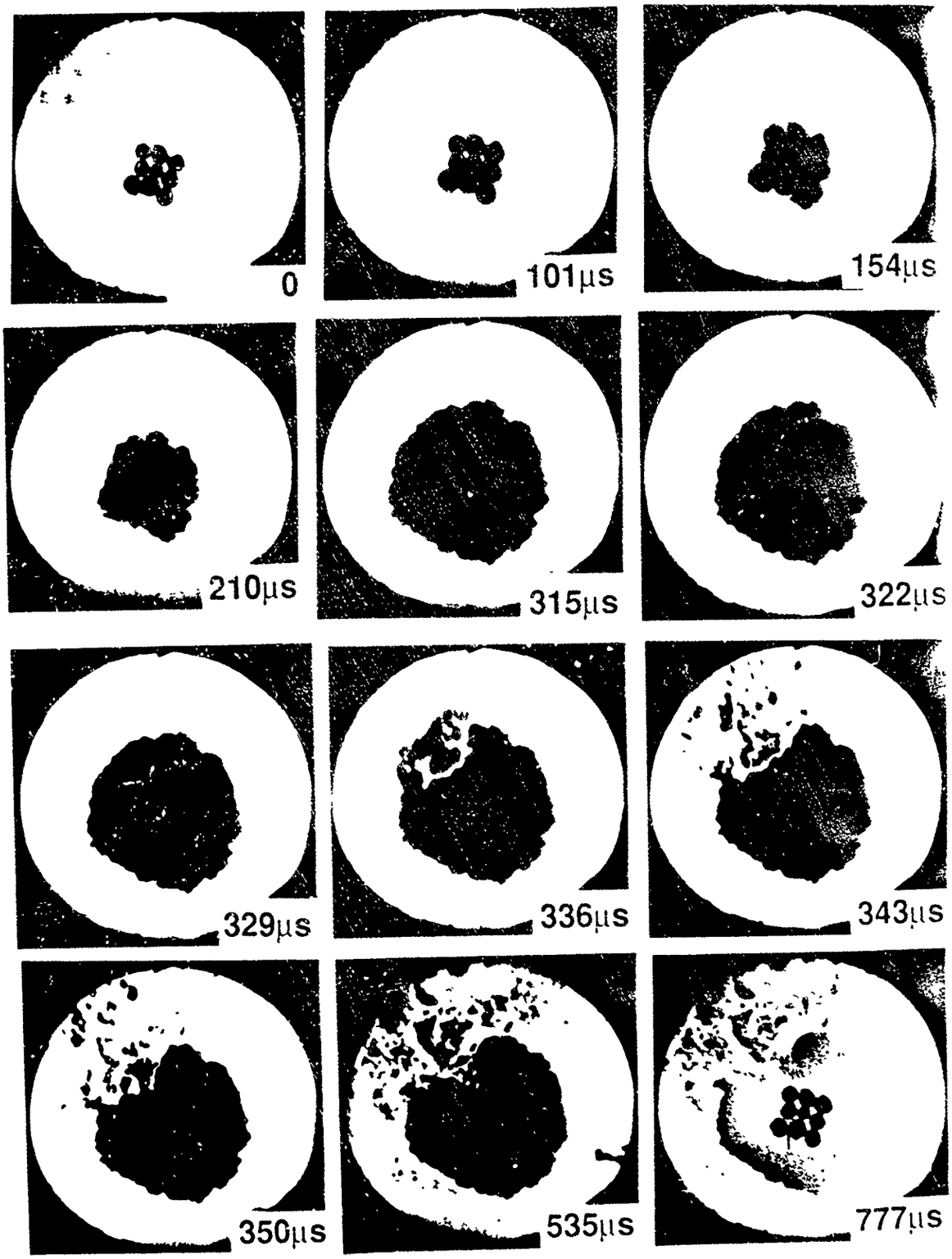

Figure 2. Selected frames from a high-speed photographic sequence of the rapid deformation of a 3×3 array of propellant composition P4.

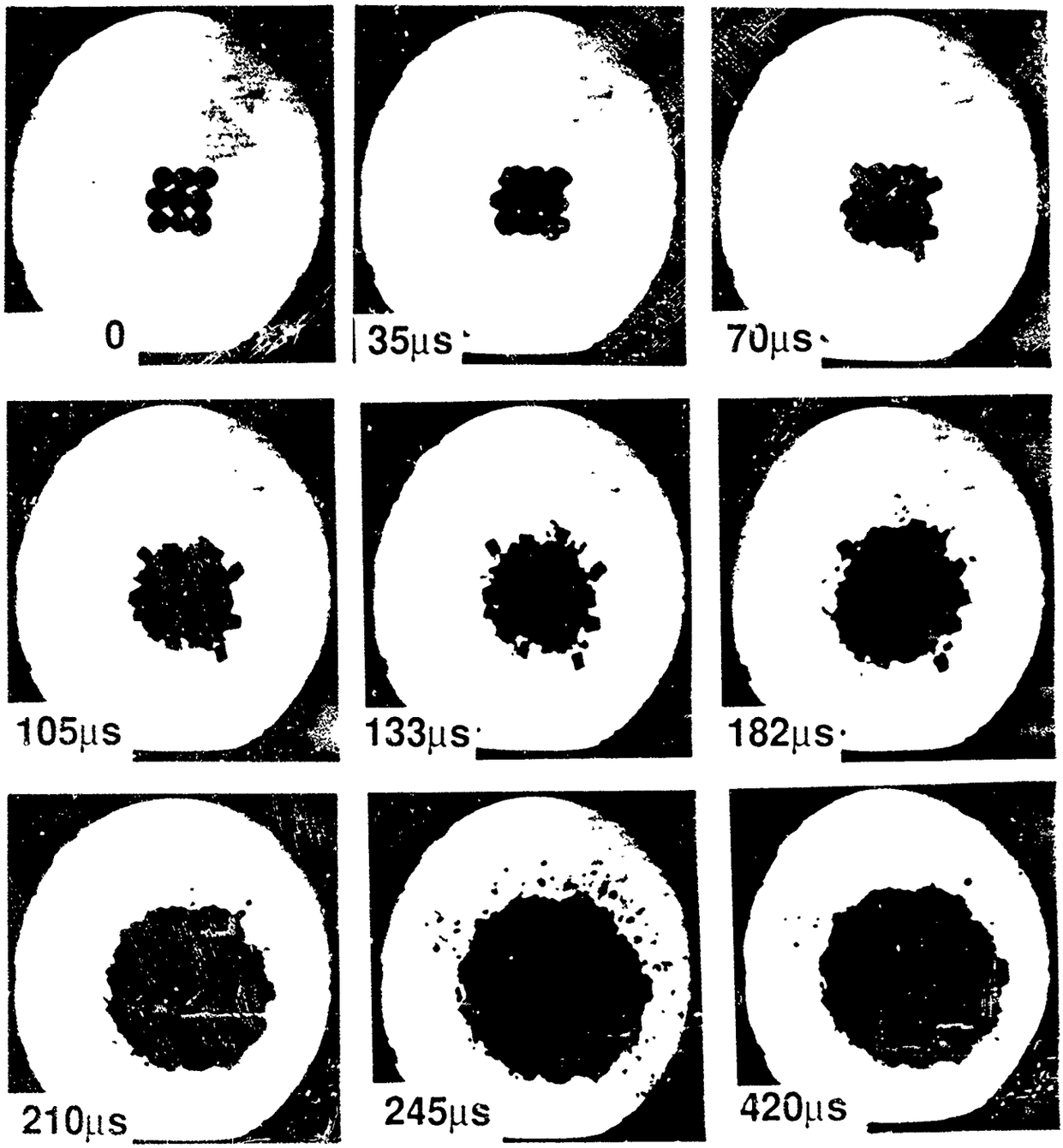

Figure 3. Selected frames from a high-speed photographic sequence of the rapid deformation of a 3×3 array of propellant composition P5.

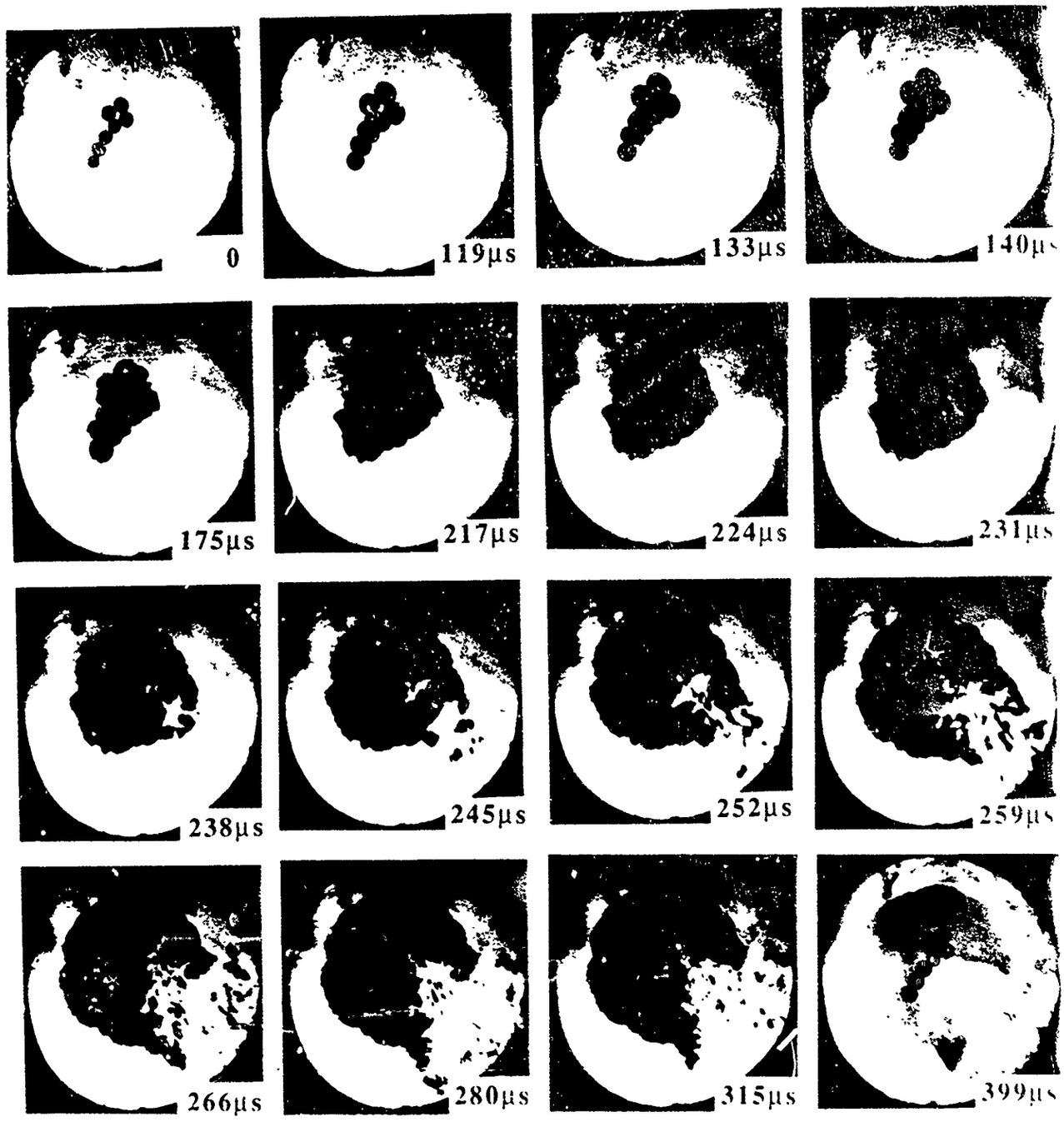

Figure 4. Selected frames from a high-speed photographic sequence of the rapid deformation of a cross-shaped array of propellant composition P1.

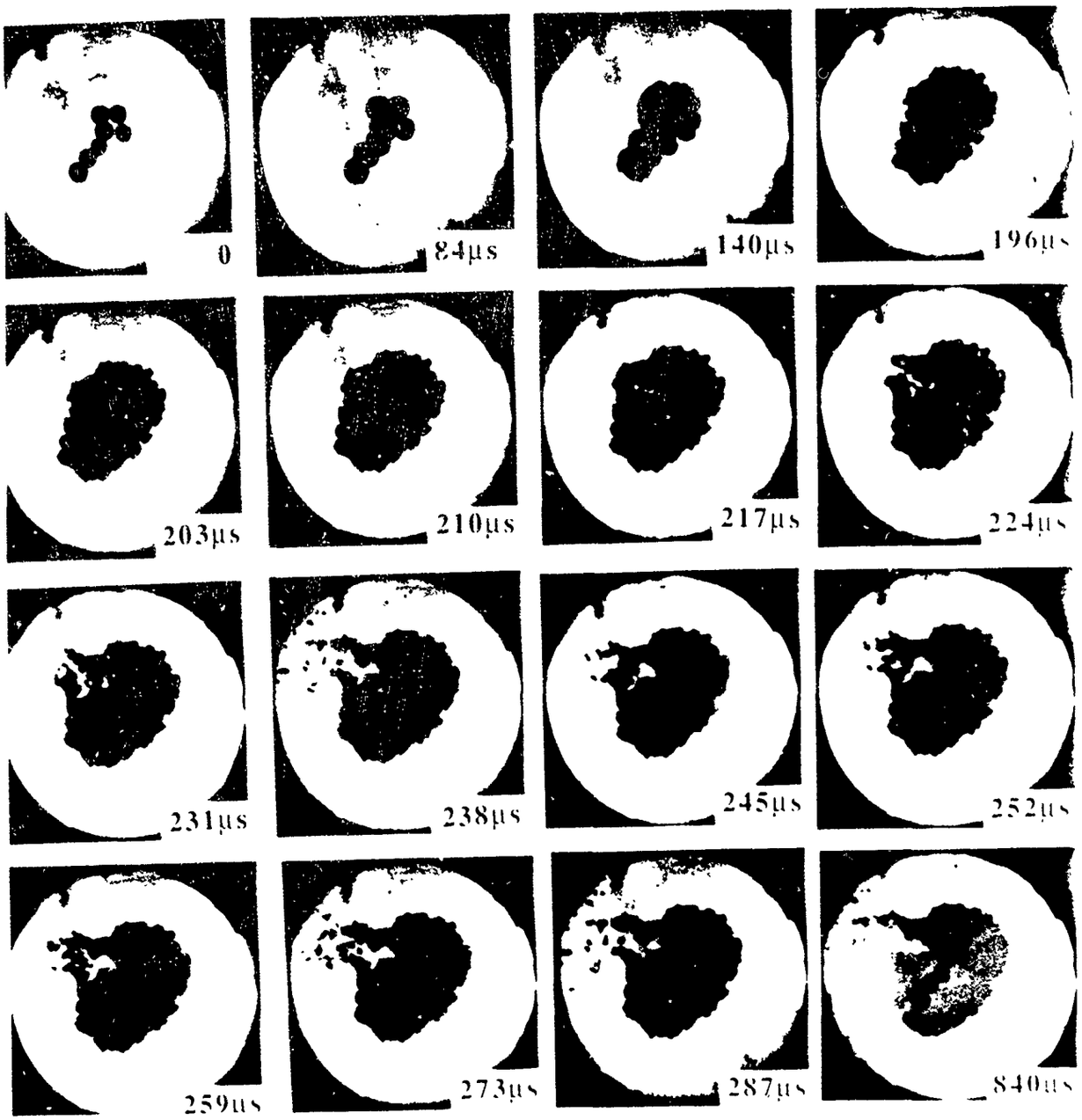

Figure 5. Selected frames from a high-speed photographic sequence of the rapid deformation of a cross-shaped array of propellant composition P4.

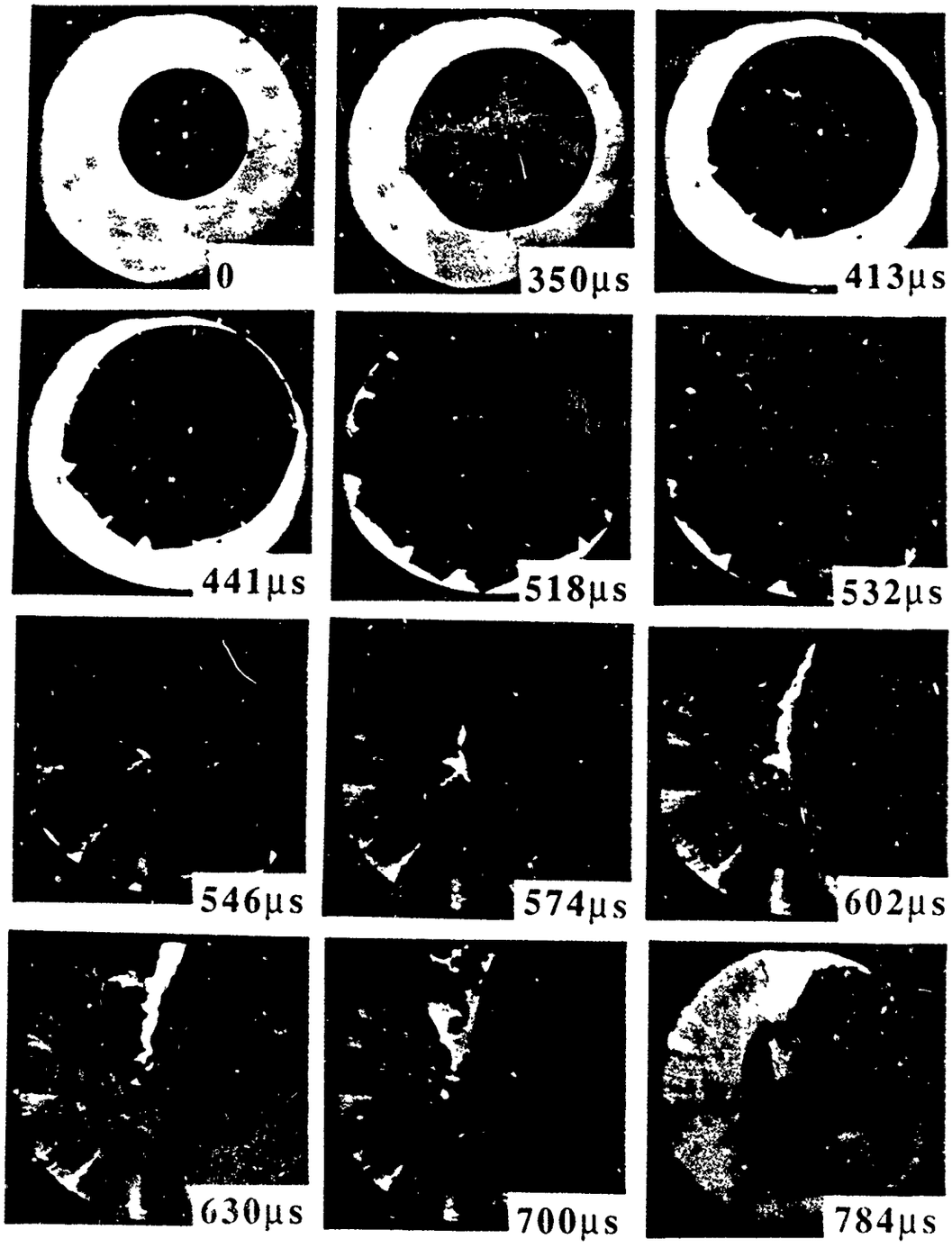

PROPELLANT 1
2 mm THICK

Figure 6. Selected frames from a high-speed photographic sequence of the rapid deformation of a 2mm thick disc cut from a slotted tube made from a conventional propellant composition.

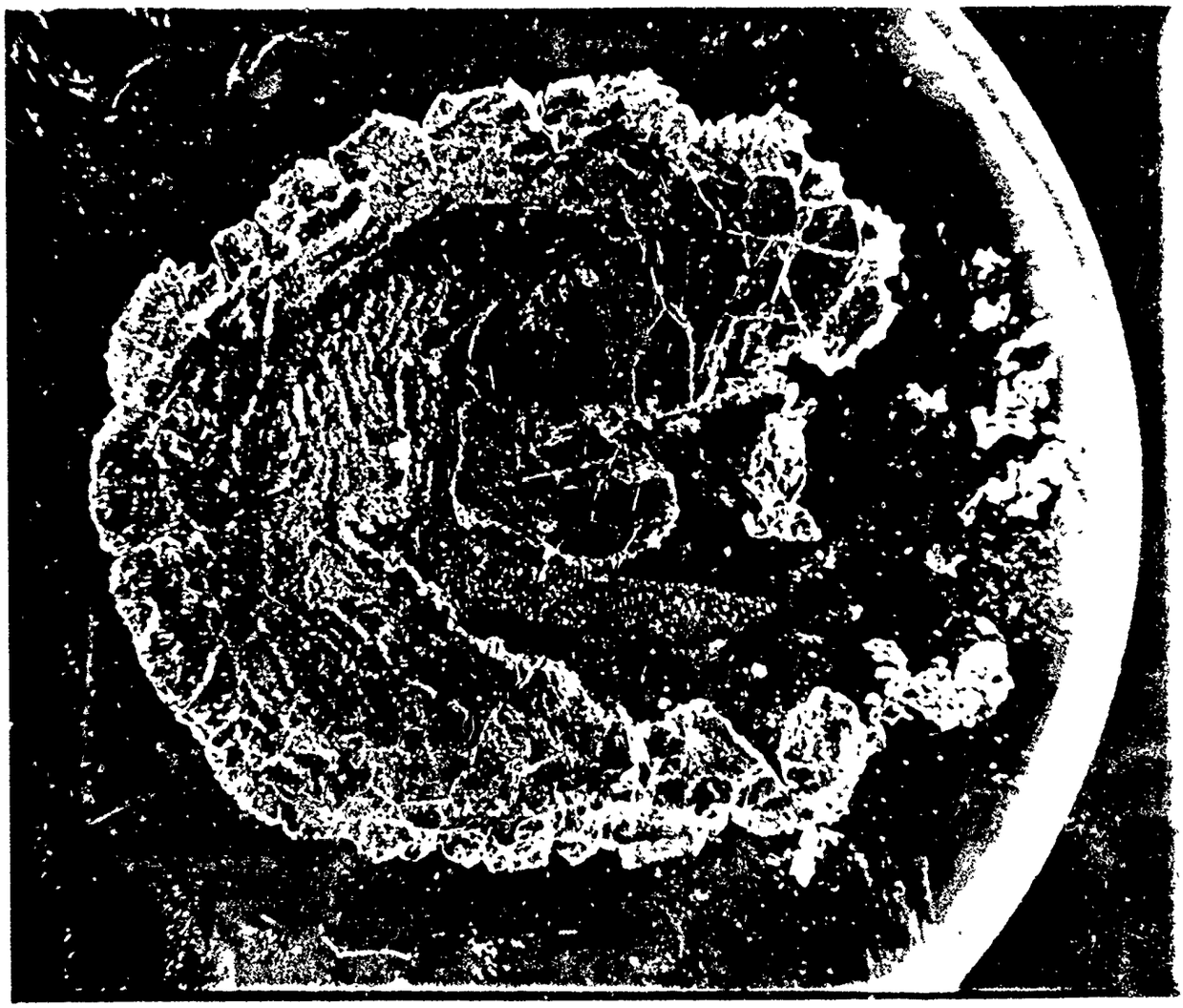

Figure 7. Damage marks on the glass anvil due to the deflagration event shown in figure 6.

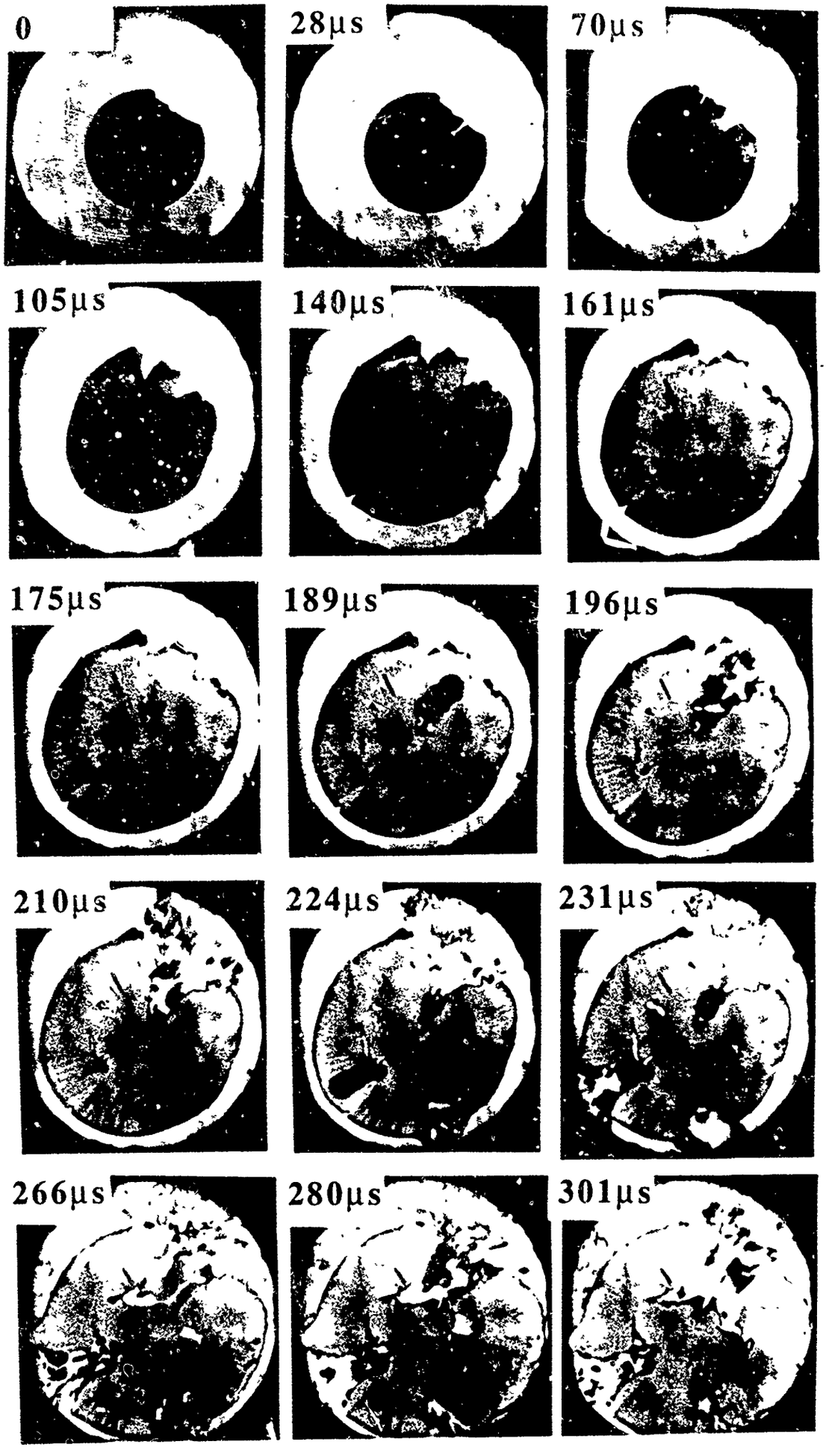

Figure 8. Selected frames from a high-speed photographic sequence of the rapid deformation of a 1mm thick disc cut from a slotted tube made from a conventional propellant composition.

Figure 9. Damage marks on the glass anvil due to the deflagration event shown in figure 8.

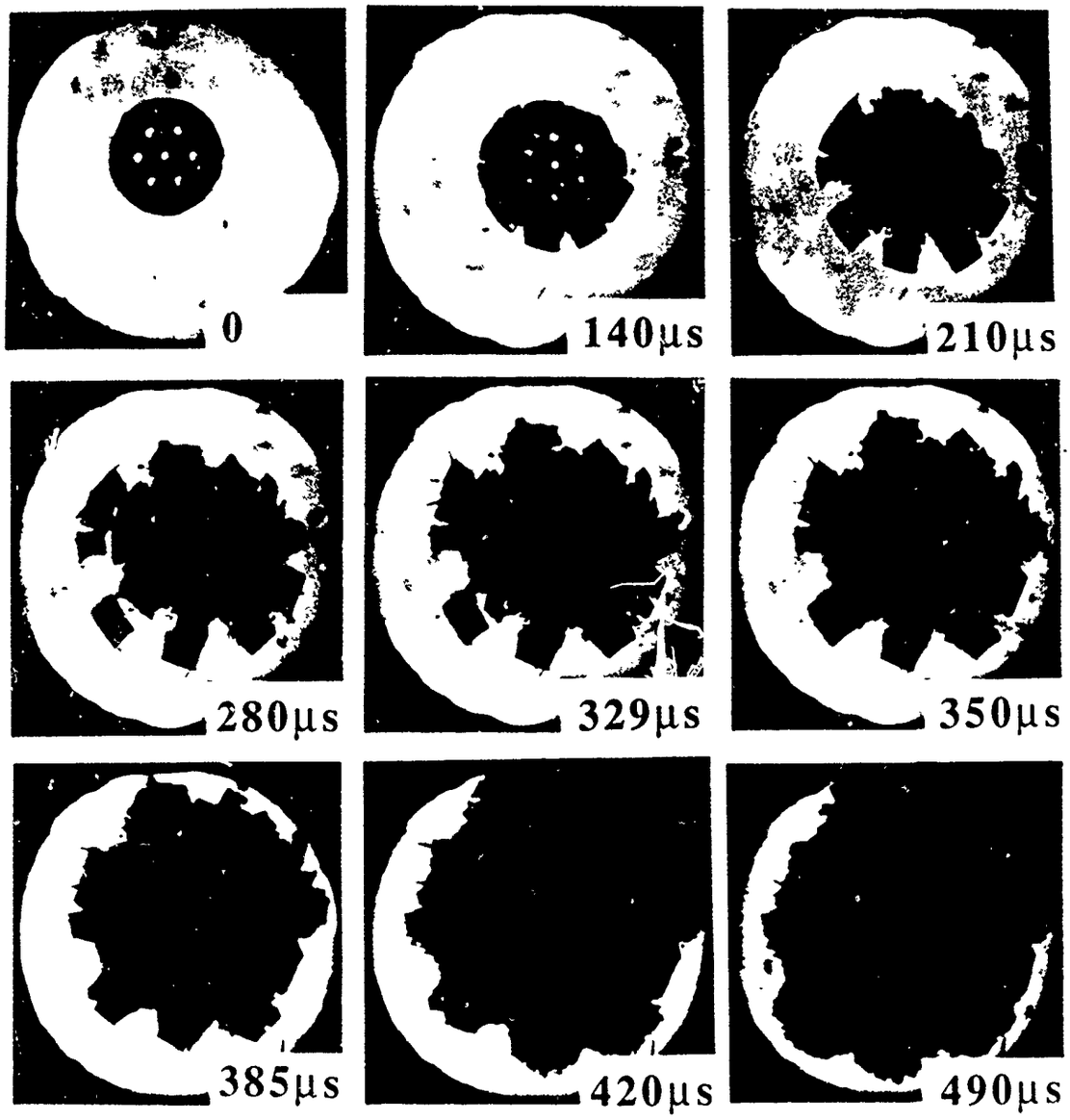

Figure 10. Selected frames from a high-speed photographic sequence of the rapid deformation of a 2mm thick disc made from a low vulnerability propellant composition.

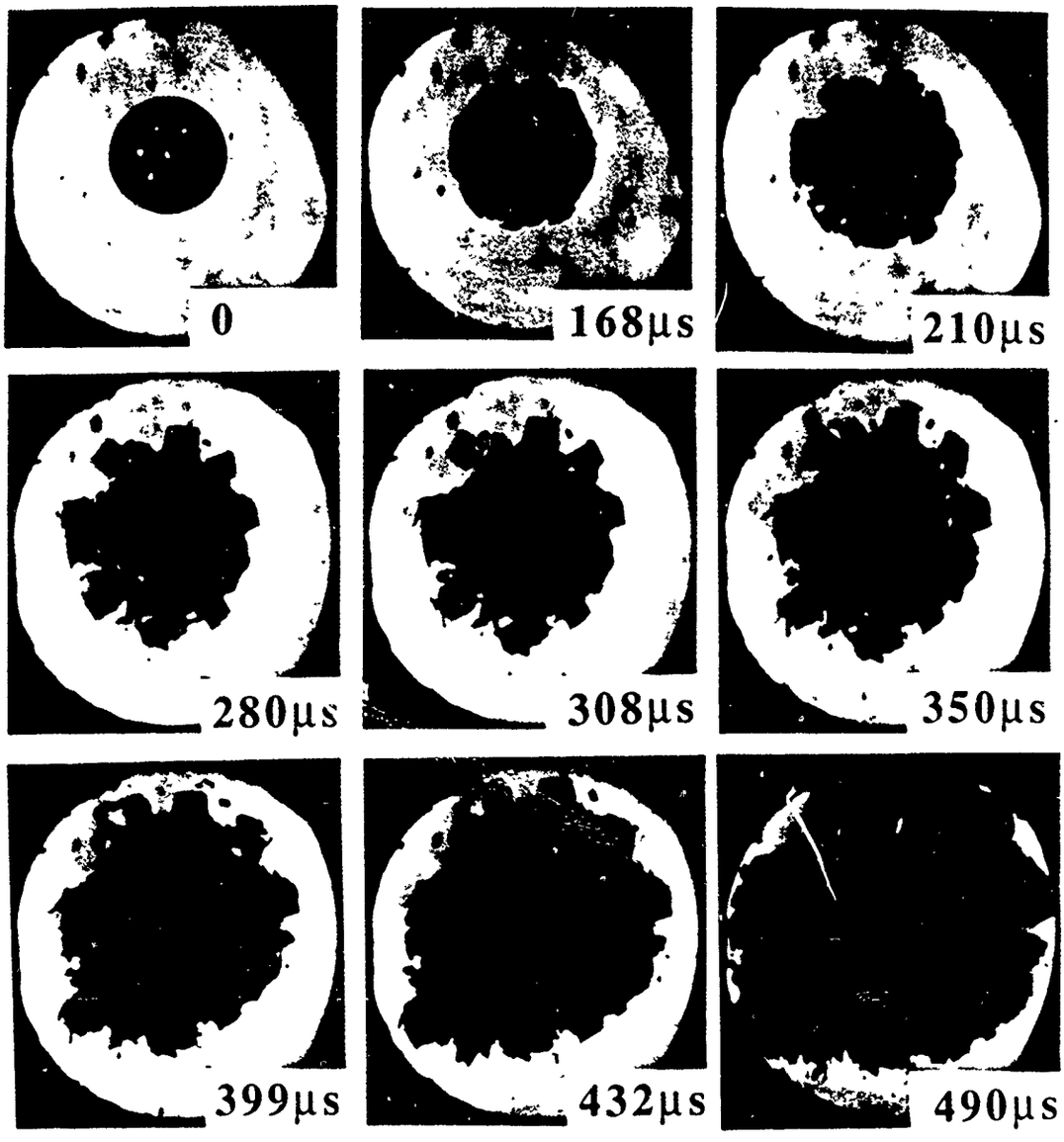

Figure 11. Selected frames from a high-speed photographic sequence of the rapid deformation of a 2.5mm thick disc made from a low vulnerability propellant composition.

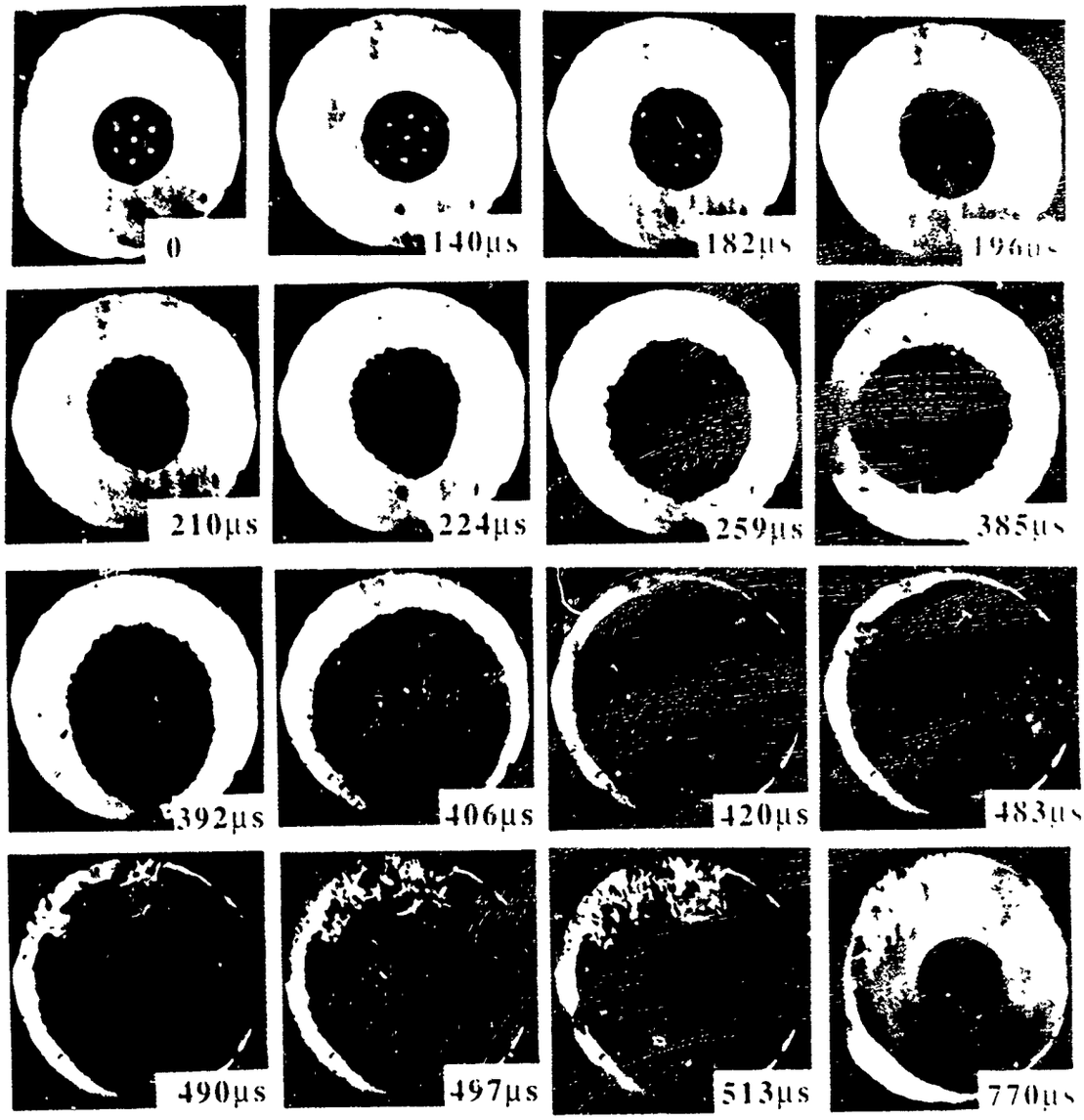

PROPELLANT 2
0.5mm THICK

Figure 12. Selected frames from a high-speed photographic sequence of the rapid deformation of a 0.5mm thick disc made from a low vulnerability propellant composition. Deflagration occurred.

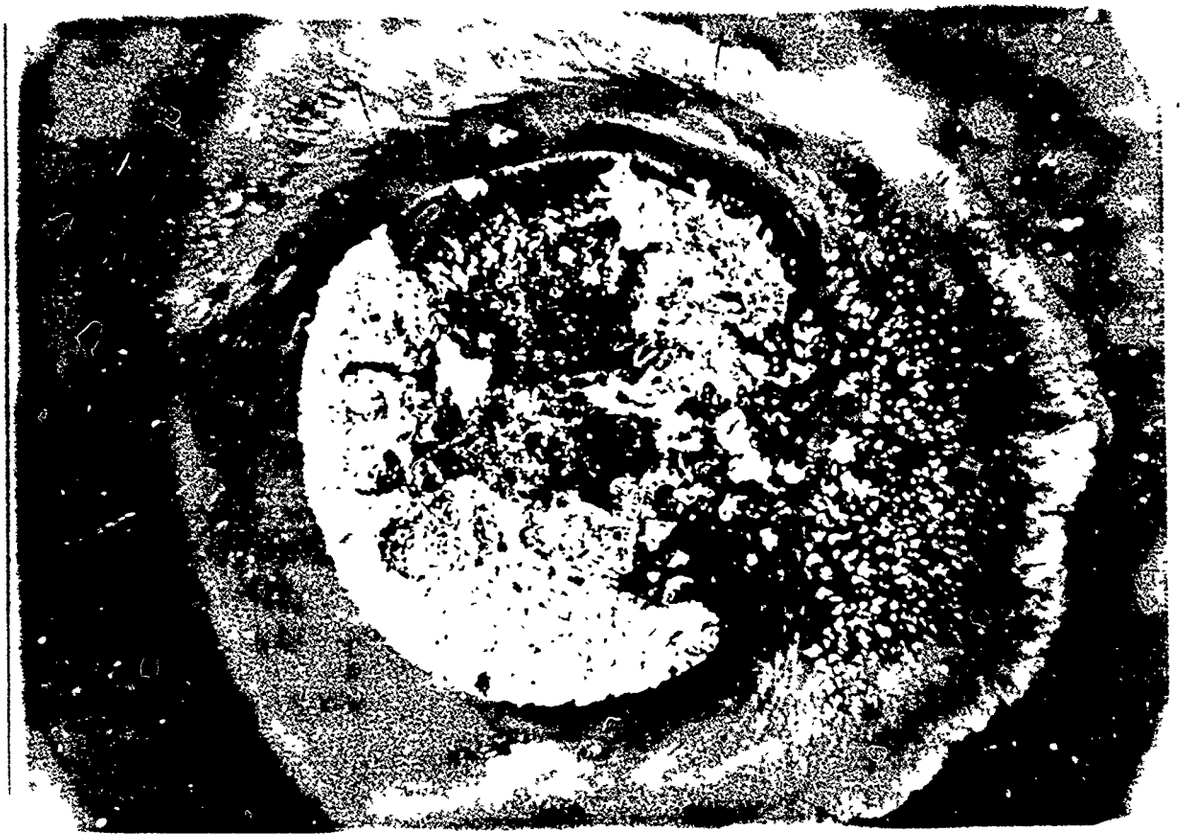

Figure 13. Damage marks on the glass anvil due to the deflagration event shown in figure 12.

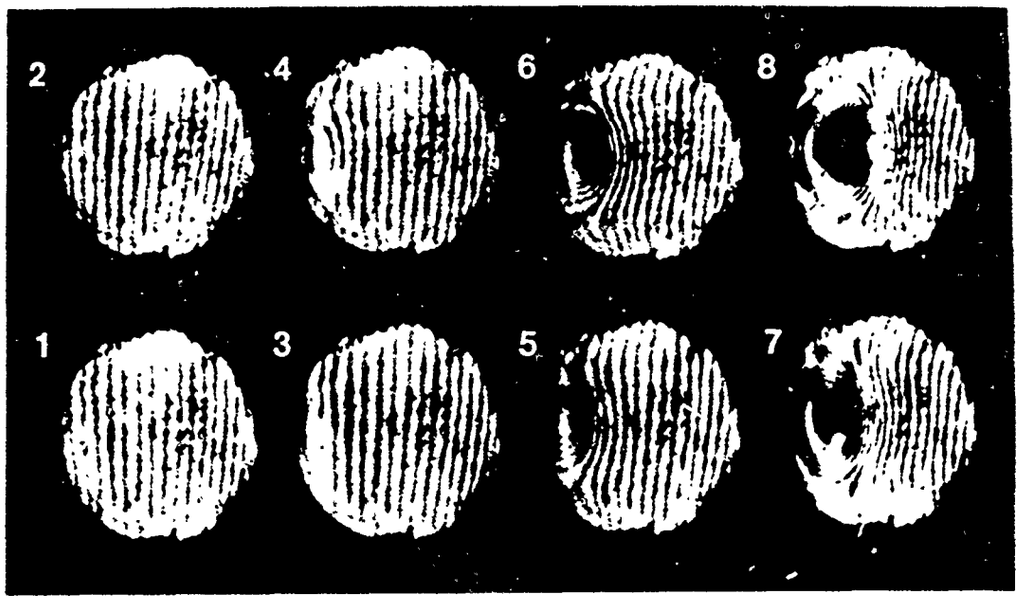

Figure 14. High speed moiré sequence of the central region (diameter 22.2 mm) of a composite disc undergoing impact by a slider from left to right. Rubber thickness = 0 mm. Interframe time = 5 μs.

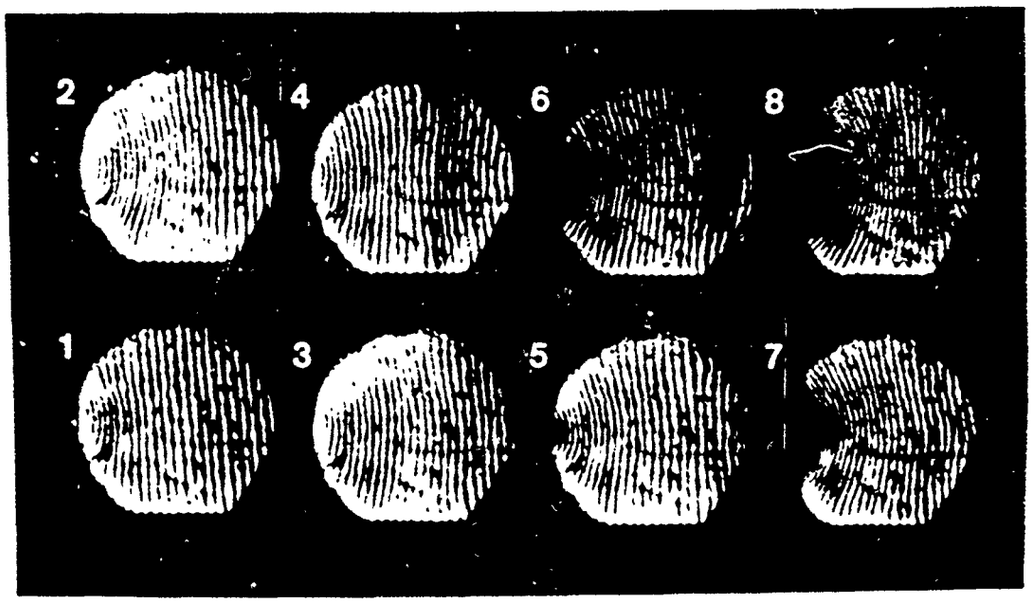

Figure 15. High speed moiré sequence of the central region (diameter 19.1 mm) of a composite disc undergoing impact by a slider from left to right. Rubber thickness = 1.55 mm. Interframe time = 5 μs.

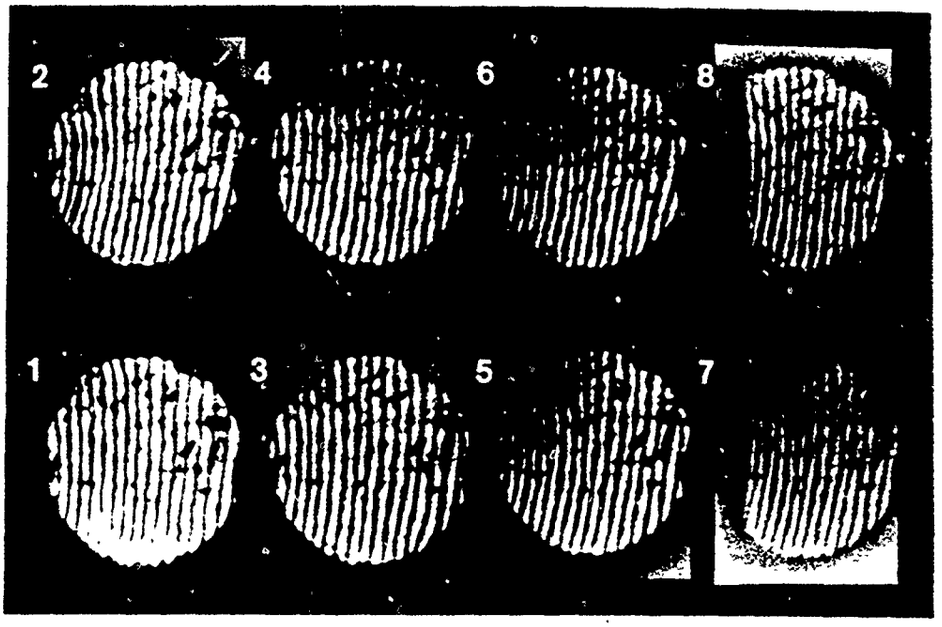

Figure 16 High speed moiré sequence of the central region (diameter 15.9 mm) of a composite disc undergoing impact by a slider from left to right. Rubber thickness = 3.15 mm. Interframe time = 5 μs.

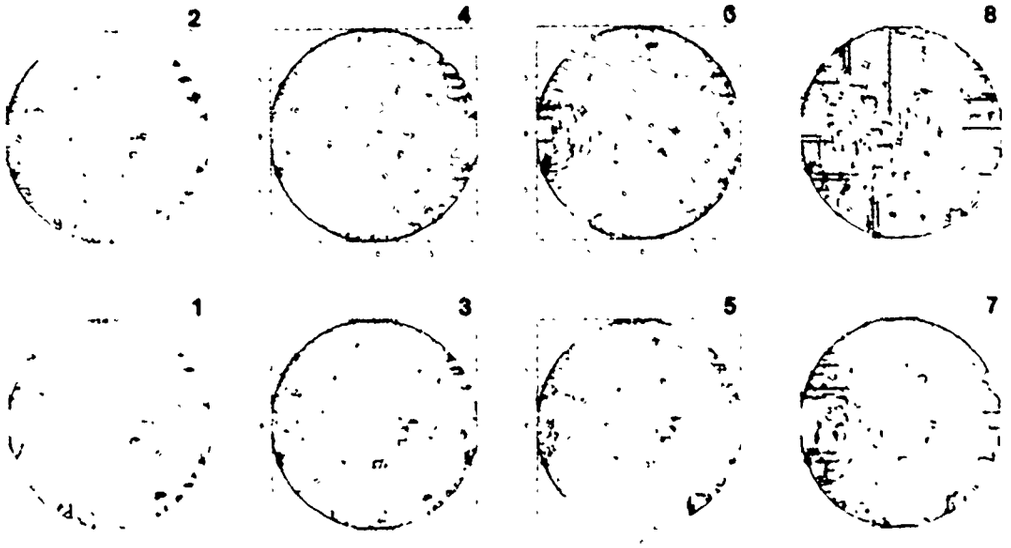

Figure 17. Contours of the horizontal displacement component for the high speed sequence in Fig. 15. Contour interval = 2 μm.

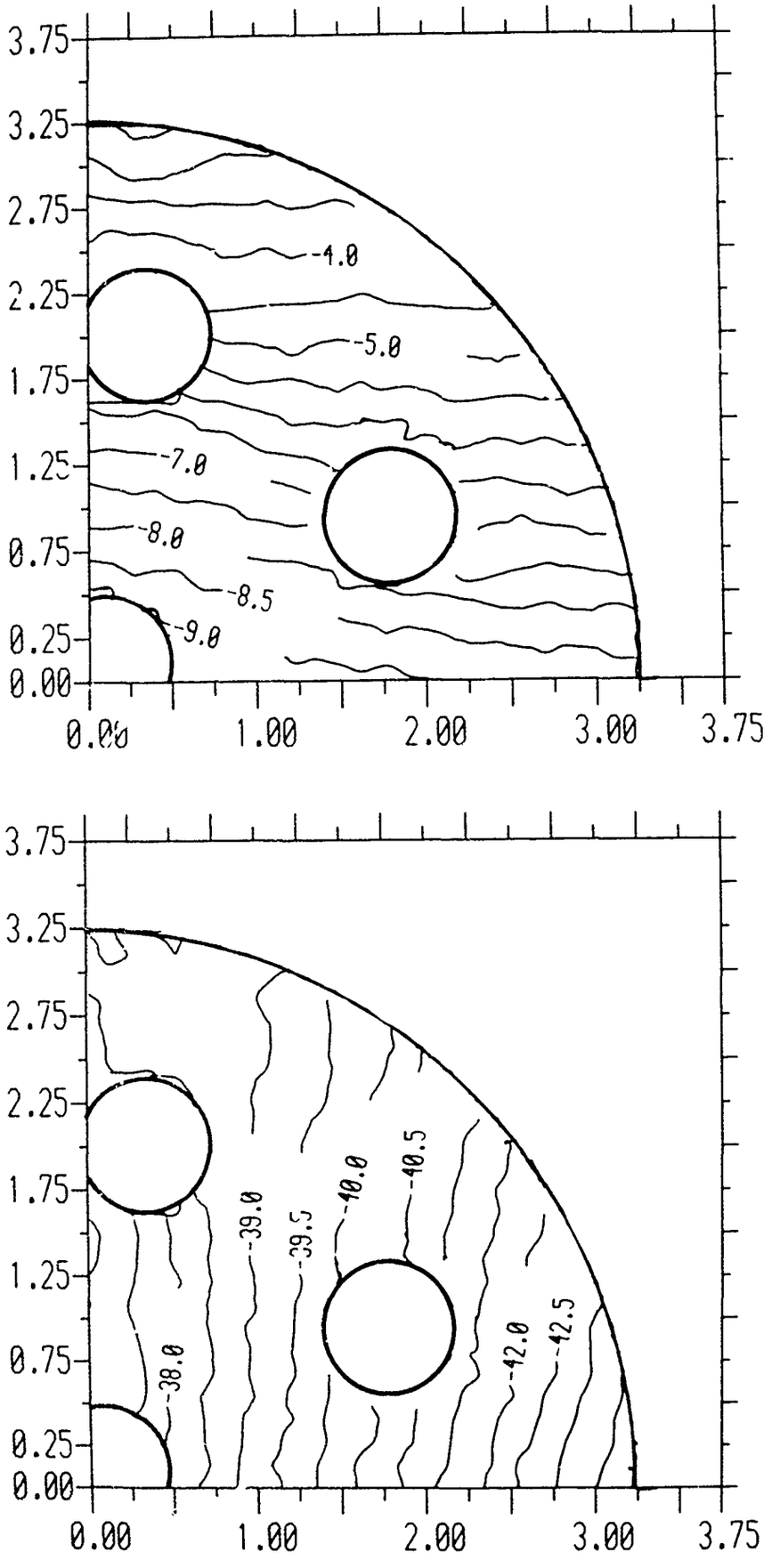

Figure 18. Contour plots showing the in-plane displacement components U_x and U_y parallel to the X and Y axis respectively at a load of 22.9 kg.

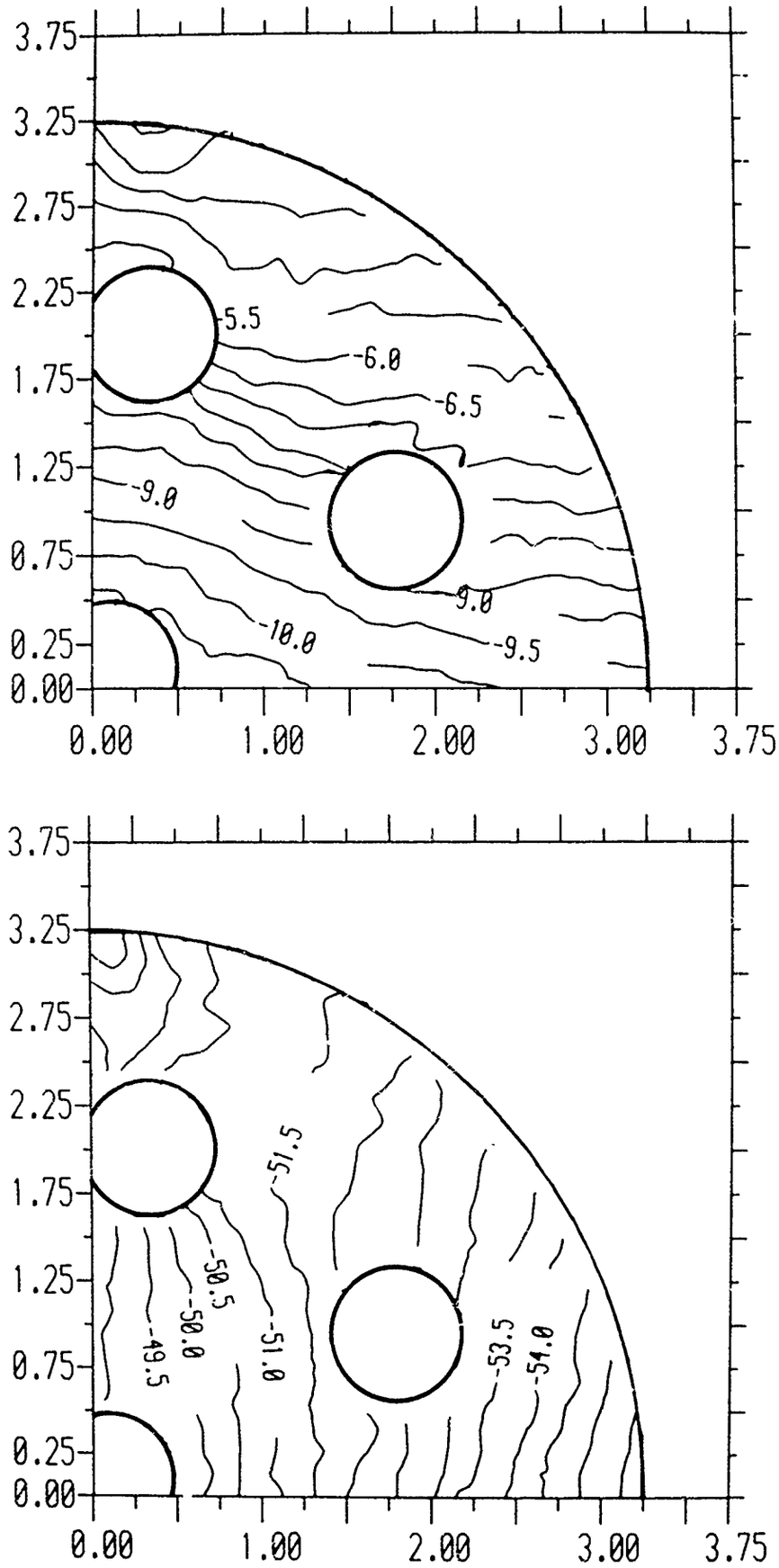

Figure 19. Contour plots showing the in-plane displacement components U_x and U_y parallel to the X and Y axis respectively at a load of 30.5 kg.

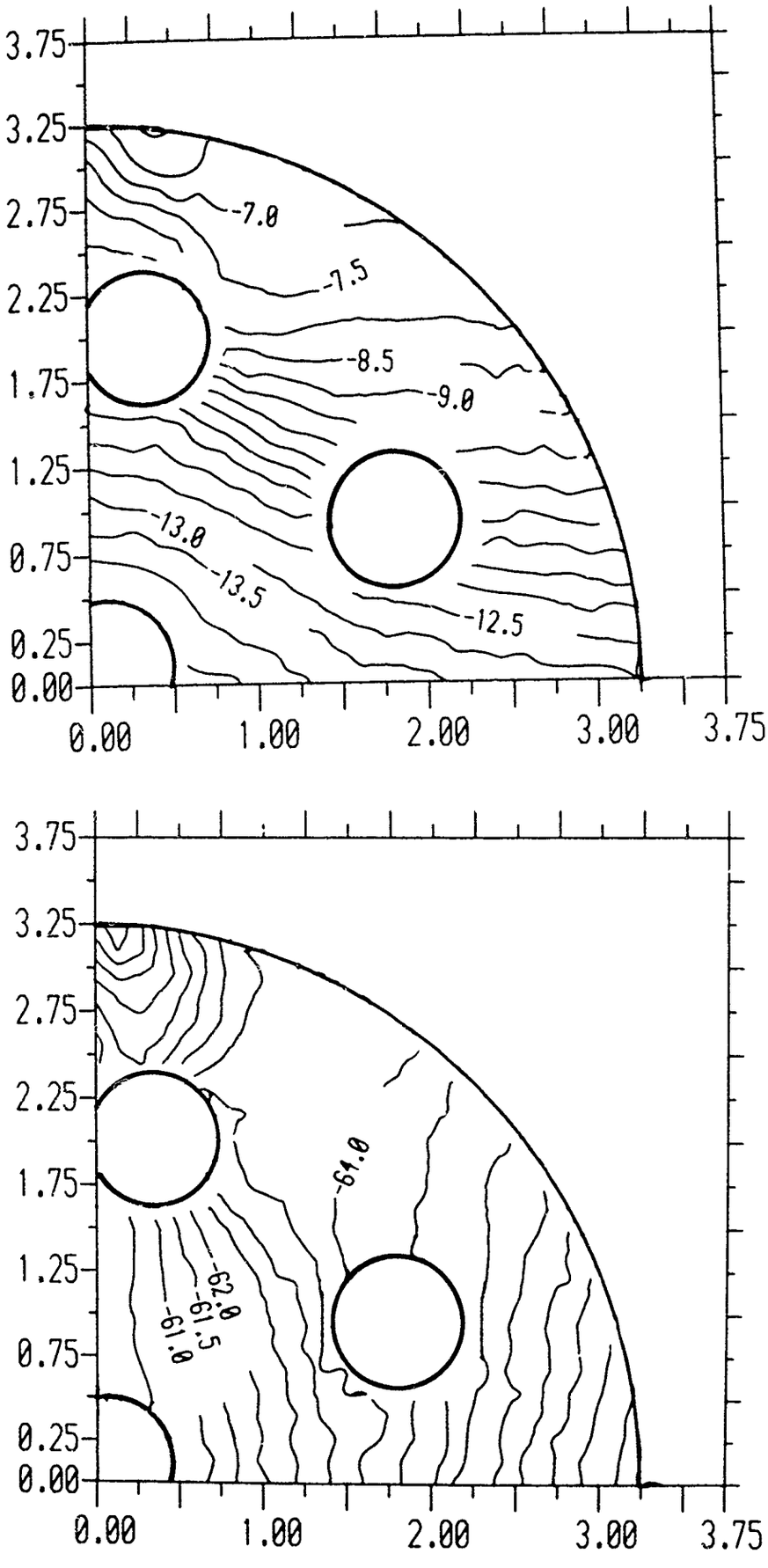

Figure 20. Contour plots showing the in-plane displacement components U_x and U_y parallel to the X and Y axis respectively at a load of 31.9 kg.

TATB/HMX/KEL-F
85/10/5

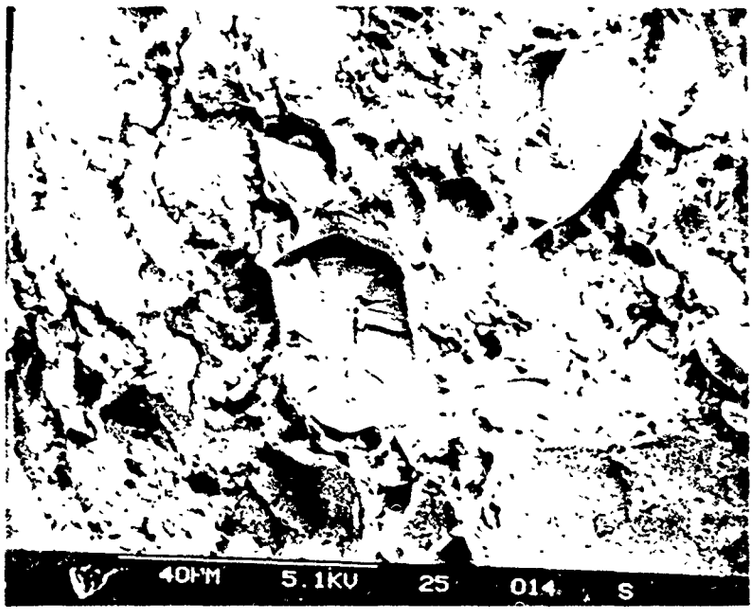

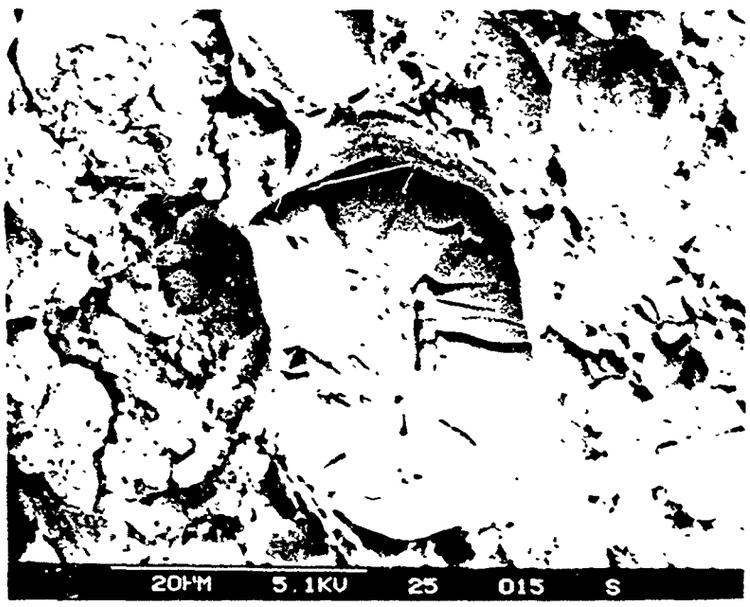

Figure 21. SEM micrographs of the cleavage fracture of a crystal, showing surface steps on the fracture surface.

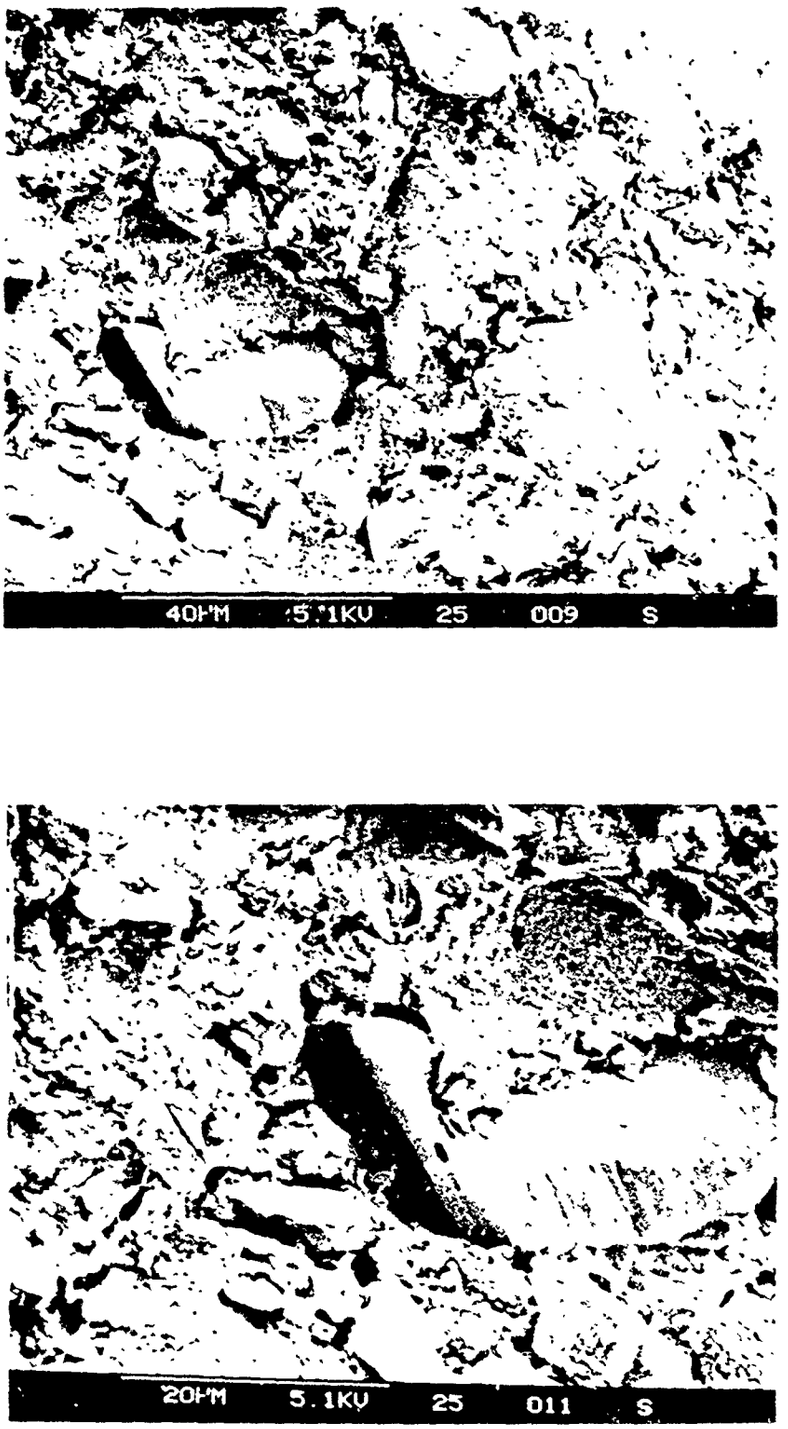

Figure 22. SEM micrographs showing a twinned crystal, probably of TATB,underneath a layer of polymer. Also note the impressions left behind by debonded crystals.

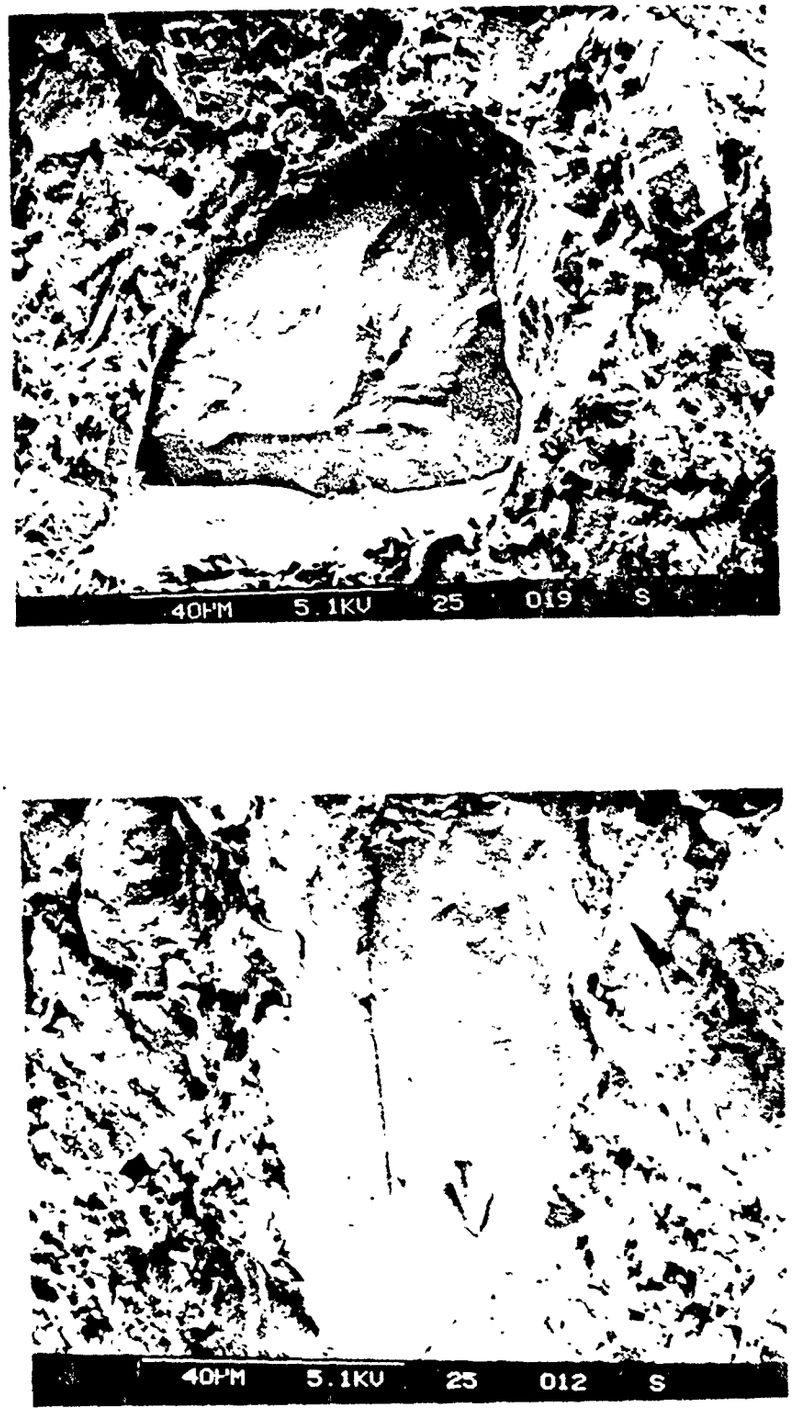

Figure 23. SEM micrographs showing two examples of fractured crystals. In both cases part of the crystal is missing, leaving behind a hole.

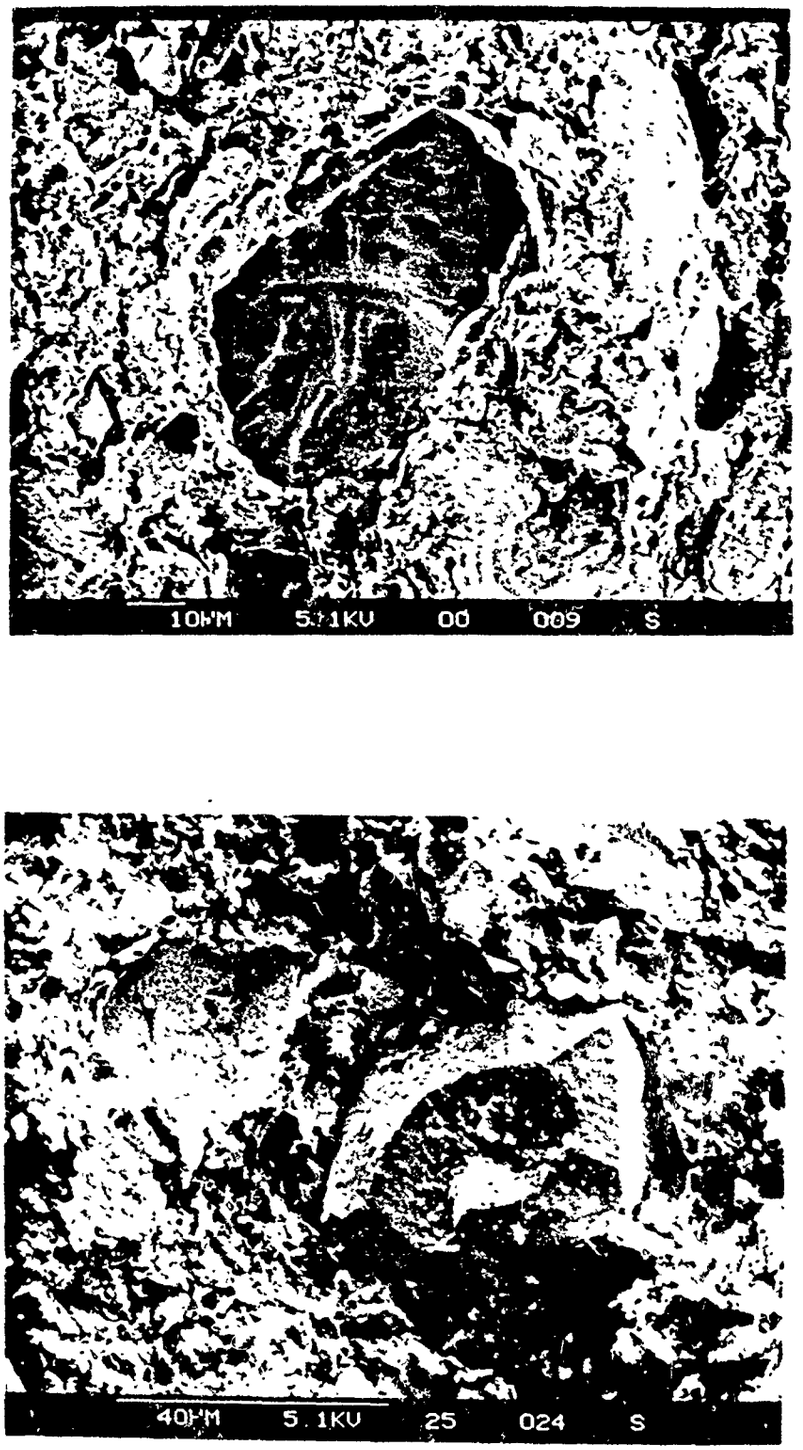

Figure 24. SEM micrographs showing a large 60 μm fractured crystal in the top micrograph. The lower micrograph shows a partially debonded crystal, with small particles of binder adhering to the angular faces.

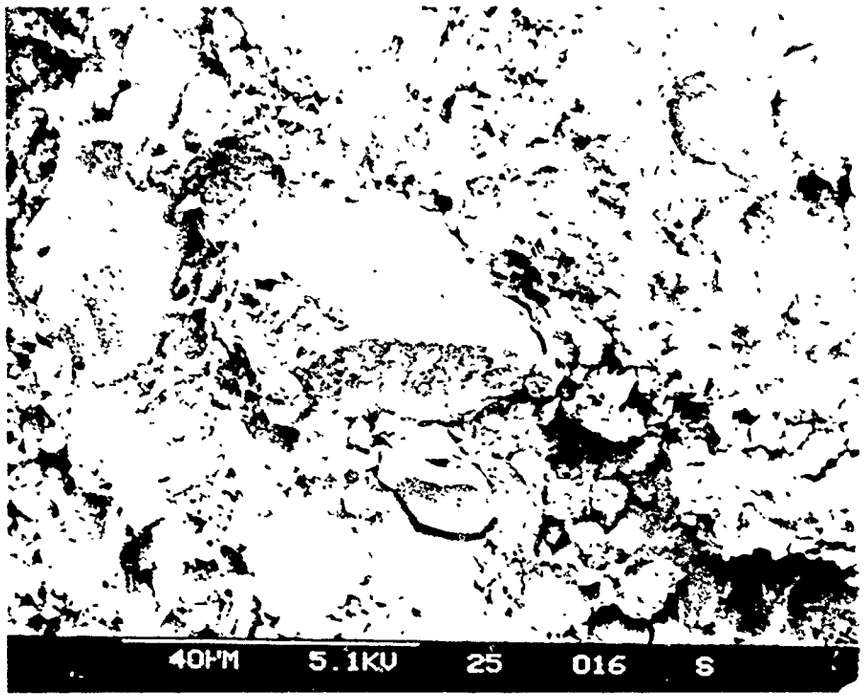

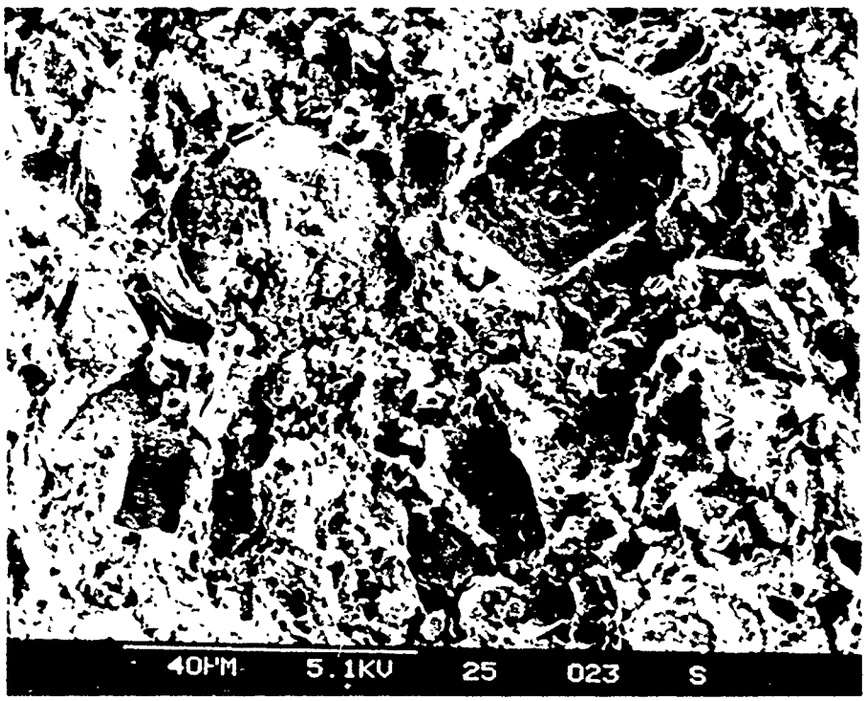

Figure 25. SEM micrographs showing partially debonded crystals.

Figure 26. Montage showing the fracture route through a sample of HMX/HTPB, fractured in the Brazilian test after polishing and staining. Note the interfacial failure at the sites of the large crystals.

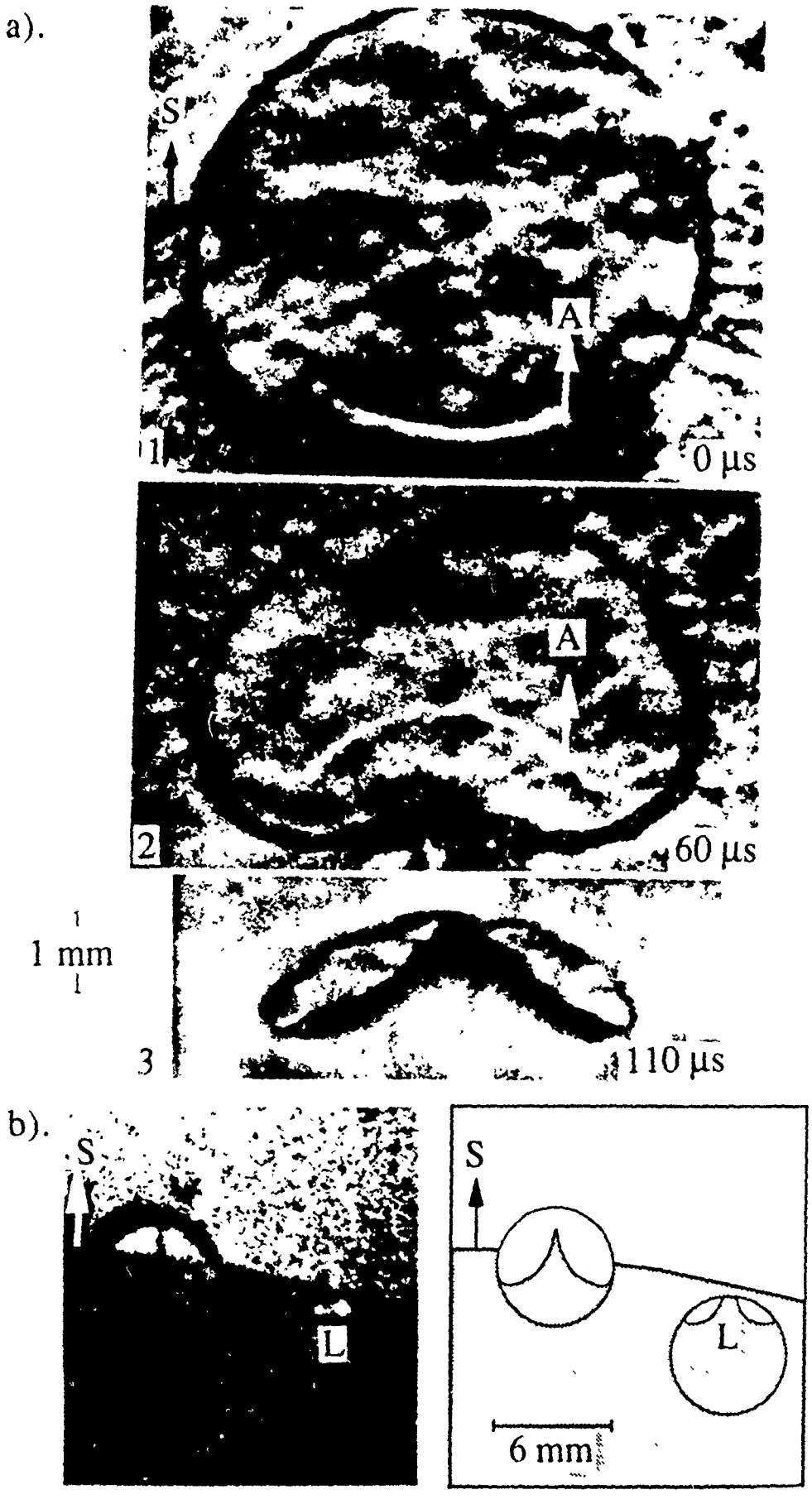

Figure 27. The asymmetrical collapse of cylindrical, air filled bubbles in gelatine. (a). The incident shock, S, of pressure 0.26 GPa, collapses a 12 mm cavity. Note the air shock, A, bouncing within the cavity and the formation of a jet which impacts in frame 3 isolating two lobes of trapped gas. (b) the shock, of strength 1.88 GPa, collapses a 6 mm cavity. The jet is crossing the left-hand cavity faster than the incident shock is moving. A second cavity on the right has already collapsed and two points of light are seen from the trapped lobes of luminescing gas.

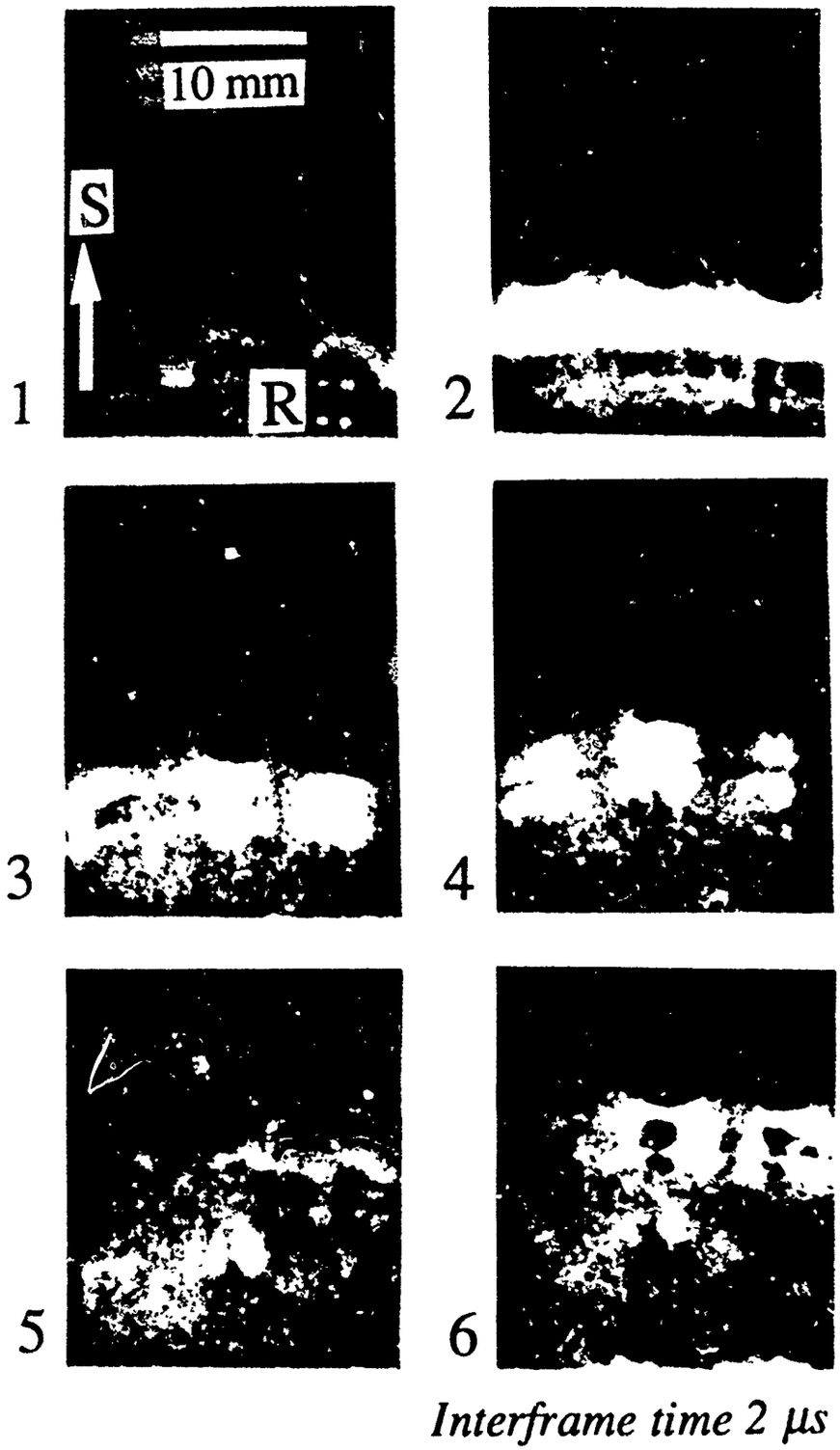

Figure 28. The collapse of a 3×3 square array of 5 mm cavities punched into the emulsion. The shock, S, enters from below causing two points of reaction, R, on the upstream wall. A double image occurs here and with other reaction sites because of refraction through the shock in the confining blocks. Collapse of the array proceeds row by row with reaction sites ahead of the incident shock. The average lifetime of sites is 5 μs. The sequence is unlit.

APPENDIX 1

Proc. Intl Conf. Hologram Interferometry and Speckle Metrology,
November 5-8, 1990, Baltimore, USA

AUTOMATIC SPECKLE PHOTOGRAPHY FRINGE ANALYSIS: APPLICATION TO ELECTRON MICROSCOPY AND HIGH SPEED PHOTOGRAPHY

J.M. Huntley, M.B. Whitworth, S.J.P. Palmer,
H.T. Goldrein and J.E. Field

University of Cambridge, Cavendish Laboratory,
Madingley Road, Cambridge CB3 0HE, U.K.

ABSTRACT

A new method of analysing the Young's fringe patterns from a double exposure speckle photograph is proposed, based on maximum likelihood estimation. Unlike previous linear algorithms, which rely on Fourier spectral analysis, the method allows knowledge of the speckle noise statistics to be incorporated in a systematic way. As a result, random errors in the measured displacement components are reduced, in the case of good visibility fringe patterns by a factor of up to six times. The use of an automatic image processing system in experimental mechanics is illustrated with two novel applications of speckle photography. The white light speckle technique has been combined with scanning electron microscopy to measure displacement fields around crack tips in aluminium with submicron sensitivity. In the second example, it is shown how a ruby laser can be repetitively Q-switched, and synchronised to a rotating mirror camera to record laser speckle photographs at microsecond framing rates.

INTRODUCTION

Double exposure speckle photography is a wholefield technique for measuring in-plane displacements in solid and fluid mechanics. In its original form,[1] the technique involves photographing the speckle pattern created by scattering a laser beam off the specimen surface. Two exposures are recorded on the same film, and the displacement field occurring between the exposures is mapped out by measuring the speckle displacement point by point from the photograph. This measurement is normally done by probing the photograph with a narrow laser beam: the spacing and angle of the Young's fringes which modulate the diffraction halo determine the local displacement vector. These basic principles can also be applied to photographs recorded by incoherent illumination (white light speckle photography), provided a suitable artificial speckle pattern is applied to the specimen surface.[2] In both cases, the sensitivity (minimum measurable displacement) is controlled by the speckle diameter, σ. For laser speckle, the value of σ in the image plane is

$$\sigma = 1.2 \lambda F (1+M) \qquad (1)$$

F is the aperture ratio of the objective lens, M is the magnification, and λ is the wavelength of the illumination. For white light speckle, σ tends to be higher than the value given by equation (1) due to lens aberrations and defocus.

The analysis of one speckle photograph involves measuring typically several hundred Young's fringe patterns. Automation of such a repetitive task is highly desirable. However, estimation of the two spatial frequency components, (k_m, k_n) of the fringes from a digitised pattern is not a straightforward process because of the noise which modulates the fringes. Techniques have been proposed based on integration of the fringes along the fringe direction,[3-6] or on averaging the 1-D autocorrelations of the rows and columns of the image,[6] to produce 1-D signals with reduced noise level. Two-dimensional Fourier[7] and Walsh[8] transforms have also been used to identify the spatial frequency components directly. The performances of these four algorithms were compared in Ref. [9]. It was found that the systematic errors were negligible, and that the random errors, e, in the image plane were given by

$$e = 0.22 \sigma^2 / V R \qquad (2)$$

for the 2-D Fourier transform method, where R is the radius of the laser probe used to form the Young's fringes, and V is the fringe visibility. Random errors for the other three techniques were on average 5-24% higher.

In this paper, we describe a new method based on maximum likelihood estimation. Unlike the previous linear algorithms, the method allows knowledge of the speckle noise statistics to be incorporated in a systematic way. As a result, random errors in the measured displacement components are reduced from the value given by equation (2), in the case of good visibility fringe patterns by a factor of up to six times.

Two further extensions of the speckle technique are also described. Firstly, the use of a scanning electron microscope allows smaller speckles to be resolved than would be possible with an optical imaging system. Secondly, a high speed camera with illumination from a ruby laser has been used to record speckle photographs at microsecond framing rates.

MAXIMUM LIKELIHOOD ANALYSIS

The four fringe analysis methods described in the previous section give equal weight to all the pixels. However, the speckle noise in the diffraction halo is multiplicative rather than additive, so that the fringe maxima are noisier than the minima. Maximum likelihood analysis allows this information to be used to reduce the random errors in the measured displacement components.

The digitised diffraction pattern, I(m,n) (m,n = 0,1,2...N) will be modelled by the equation

$$I(m,n) = X_1 I_0(m,n) \{1 + X_2 \cos [2\pi (X_3 (m - m_0) + X_4 (n - n_0)) / N]\} \quad (3)$$

where $I_0(m,n)$ is the (noisy) diffraction halo from a single exposure photograph, and $X_1...X_4$ are unknown parameters. The centre of the fringe pattern, (m_0,n_0) is determined by the relative orientation of the image digitiser and the optic axis, and can in principle be measured exactly. This therefore represents further prior knowledge which was not used by previous algorithms.

It will be assumed that the probability density function for I_0 at any given pixel (m,n) within a single exposure diffraction halo follows the usual negative exponential statistics:[10]

$$P(I_0(m,n)) = (1 / \langle I_0(m,n) \rangle) \exp(-I_0(m,n) / \langle I_0(m,n) \rangle) \qquad I_0(m,n) \geq 0$$

$$= 0 \qquad I_0(m,n) < 0 \quad (4)$$

where $\langle\rangle$ denotes ensemble average. In the present analysis, $\langle I_0(m,n) \rangle$ will be taken to be the sampled theoretical diffraction halo,[10] alternatively, $\langle I_0(m,n) \rangle$ could be estimated by averaging halos from a single exposure photograph. The probability density function for I(m,n) is then

$$P(I(m,n)) = (1 / \langle I(m,n) \rangle) \exp(-I(m,n) / \langle I(m,n) \rangle) \qquad I(m,n) \geq 0$$

$$= 0 \qquad I(m,n) < 0 \quad (5)$$

where $$\langle I(m,n) \rangle = X_1 \langle I_0(m,n) \rangle \{1 + X_2 \cos [2\pi (X_3 (m - m_0) + X_4 (n - n_0)) / N]\} \quad (6)$$

Assuming independence between pixels, the likelihood of the observed intensity distribution is proportional to

$$L = \prod P(I(m,n)) \quad (7)$$

where the product is over all pixels within the fringe pattern. Maximum likelihood estimation involves choosing the parameters $X_1...X_4$ that maximize L, or equivalently $\ln L$:

$$\ln L = - \sum \ln \langle I(m,n) \rangle - \sum [I(m,n) / \langle I(m,n) \rangle] \quad (8)$$

The proposed method was tested on the database of 320 fringe patterns described in Ref. [9], using routine E04LAF from the NAGLIB library to minimize $-\ln L$ subject to the constraint $X_2 < 1$. The initial values of $X_1...X_4$ were chosen according to the final output from the 2-D Fourier transform method ($X_1 = [\sum I(m,n)] / [\sum I_0(m,n)]$; $X_2 = V$; $X_3 = k_m$, $X_4 = k_n$). The summation in equation (8) was over all datapoints within a radius of 120 pixels of (m_0, n_0), but excluding the undiffracted beam. The random errors are plotted as functions of V and R in Figs. 1 and 2, respectively, for comparison with the performance of the other four algorithms. The greatest relative reductions occurred with the fringes of highest visibility: by a factor of 6 at visibilities approaching unity. However, even at V = 0.2, the errors were still 30% lower than the 2-D Fourier transform values.

WHITE LIGHT SPECKLE WITH THE SCANNING ELECTRON MICROSCOPE

When recording speckle photographs, the use of a small speckle diameter is generally desirable, since this improves the sensitivity and accuracy of the technique. The speckle diameter in the specimen plane is $1.2\lambda F(1+M)/M$ (see equation (1)), which has a minimum value $1.2\lambda F$ at high magnification. This is typically 1 μm or more at optical wavelengths. The use of a scanning electron microscope (SEM) brings two substantial advantages: a lower operating wavelength, and hence improved resolution; and increased depth of field. Speckle photography with an electron microscope was suggested by Chiang and Li[11]. In this section, we briefly review a more detailed study of the use of a SEM for speckle photography at high magnification; further details may be found in Ref. [12].

A number of surface treatments were tried, including latex beads and sputtered gold,[11] but the best speckle patterns consisted of magnesium oxide crystals, created by burning magnesium ribbon in air. The natural size of the crystals is about 0.5 μm, as shown in Fig. 3, but this may be increased by burning the magnesium in a more humid environment. When recording the speckle photographs, the magnification is chosen such that the speckle diameter is comparable to the distance between scan lines of the microscope. As is usual practice in electron microscopy, the sample surface is made conducting by application of a thin coating of gold.

To illustrate the technique, Fig. 4 shows a double exposure speckle photograph of a notched aluminium specimen under mode I loading. The notch is oriented vertically with respect to the micrograph, with the tip (radius 0.15 mm) just below the centre of the lower edge. The microscope was a Cambridge Stereoscan 250 Mk2. The straining stage was made of brass, to prevent interference with the electron beam, and was designed to load the specimen symmetrically. In practice, some rigid body movement still occurred during straining, but this was easily compensated for by repositioning the specimen between exposures. The film used was Ilford FP4; after development, the negatives were contact printed onto a high-contrast film (Ilford Technical line film) to improve the fringe visibilities during pointwise analysis.[13]

Fig. 5 shows a Young's fringe pattern from a micrograph of a specimen under load. The laser probe radius, R, was 0.95 mm, so that the probe covered 0.56% of the total micrograph area; the equivalent probe diameter (i.e. spatial resolution) in specimen coordinates was 15 μm. The visibility, V ≈ 40%, is typical of fringes from micrographs recorded during deformation.

Fringe patterns were analysed automatically by the system described in Ref. [7], but with slight modifications to allow R to be easily varied.[12] The overall random error of the system was measured by analysing a double exposure micrograph of a rigid body displacement. The expected displacement error in specimen coordinates, calculated from equation (2) with $\sigma = 0.5$ μm, V = 0.4 and R = 7.5 μm, is $e = 18$ nm. This compares well with the measured standard deviation of 16 nm. Larger probes sample more speckles, giving a higher accuracy, but at the expense of decreased resolution.

The original 2-D Fourier transform method (64 by 64 datapoints) was reasonably reliable: the success rate with the micrograph in

Fig. 4, for example, was 96% for R=0.95 mm (7.5 μm in specimen coordinates). Failure occurred in regions of large displacement, such as at the left hand edge of Fig. 4; displacements here were up to 5 μm in specimen coordinates, which is 0.66 times the equivalent diameter of the laser probe.

To improve the reliability, the algorithm was modified to search the region $k_m^*-N_w/2 < k_x < k_m^*+N_w/2$, $k_n^*-N_w/2 \le k_y < k_n^*+N_w/2$, instead of the entire upper half of the 2-D Fourier transform plane ($k_y \ge 0$). This is a square of side N_w centred on (k_m^*,k_n^*), which is chosen to be the vector (k_m,k_n) calculated from a neighbouring interrogation point on the photograph. The choice of N_w depends on the maximum expected displacement gradient and the distance between interrogation points; the value $N_w=16$ was satisfactory for the micrograph in Fig. 4. Fig. 6 is a vector plot of the displacement field, measured from Fig. 4 on a grid of 18 by 24 datapoints. The horizontal component is replotted as a contour map in Fig. 7. The presence of a surface microcrack is clearly visible from the bunching of the contours at the right hand edge of the plot. The average strain level over the central region is about 3%.

HIGH SPEED LASER SPECKLE PHOTOGRAPHY

In this section, we describe the development of a high speed camera system for recording laser speckle photographs at microsecond framing rates. Dynamic fracture studies have already been carried out by combining the techniques of white light speckle and high speed photography[14]; however, the potential advantages of laser over white light speckle are improved sensitivity and accuracy, and reduced requirements for specimen preparation.

A Beckman and Whitley model 189 rotating mirror camera was chosen on account of its relatively high spatial resolution: 30-40 lines mm^{-1}, compared with about 10 lines mm^{-1} for most image converter cameras. The optical layout is shown in Fig. 8. The specimen is imaged onto the rotating mirror M by objective lens OL; relay lenses RL_1-RL_{25} re-image the specimen onto stationary film. Shuttering action is achieved by stops OP (near OL) and RP_1-RP_{25} at each relay lens. Field lens FL, which is situated close to the mirror, images OP onto RP_1-RP_{25}. As the mirror rotates, the image of OP coincides successively with RP_1-RP_{25}, each time exposing one frame of the film.

A pulsed ruby laser is used as the light source: most continuous wave lasers are unable to provide sufficient illumination - of the order of tens of kW - to record speckle photographs at microsecond framing rates. The laser was modified by incorporating a Pockels cell and Glan-air polariser inside the cavity. It was shown in Ref. [15] that repetitive Q-switching (modulation of the cavity losses by switching the voltage across the Pockels cell between zero and the quarter wave value) can result in a train of light pulses being emitted at the modulation frequency. Control of the laser in this way has the advantage that exposure duration is determined by the pulse width, typically only 50-100 ns, and is independent of framing rate. The main problem is that the pulses have to be synchronised with the individual frames of the camera. This is particularly important for recording double exposure speckle photographs, if the two exposures are made on separate runs of the camera. It is well known that specimen tilt between exposures results in substantial speckle decorrelation if the speckle pattern rotates by more than about 10% of the angle subtended by the lens aperture at the specimen.[16] Rotation of the camera mirror has an equivalent effect to specimen tilt; in practice, this means that as the mirror rotates, the timing of each pulse should be accurate to within about 5% of the interframe time to ensure adequate correlation of the first and second speckle patterns. To achieve this precision, a photodetector is positioned in each of the aperture stops RP_1-RP_{24}. A small flash lamp is placed in the corresponding point of aperture stop OP. The i th photodetector therefore produces a signal when the mirror is in the correct position to expose the i th frame. The output of a logical OR operation on the 24 photodetector signals is amplified and used to drive the Pockels cell.

Tests have so far been carried out with interframe times in the range 2-8 μs. It was found that in general, the energy per pulse is most uniform at high interframe times, and the fluctuations can be reduced by increasing the pump rate, and decreasing the time the Q-switch is kept open. Fig. 9 is a typical trace of the light output when the camera was operated at 8 μs $frame^{-1}$. Note that it was necessary to low-pass filter the photodiode signal because of the limited time resolution (0.2 μs) of the digital scope; the true pulse width (at half maximum) is in the range 50-100 ns. The energy per pulse is about 20 mJ.

Speckle photographs of a specimen undergoing rigid body translation were recorded onto Agfa 10E75 emulsion, at a magnification of 1.02. Fig. 10 shows a Young's fringe pattern from a photograph recorded at 2 μs $frame^{-1}$. The shape of the diffraction halo is a consequence of the rectangular geometry of the aperture plates OP and RP_1-RP_{25}. The (image plane) speckle dimensions are 6.1 and 26.0 μm in the horizontal and vertical directions, and the speckle pattern displacement is 19.9 μm. The horizontal dimension corresponds to a spatial frequency of 160 lines mm^{-1}, which is four times the claimed resolution of the camera. A region of the photograph used to produce Fig. 10 was analysed on a square grid of 6 by 6 datapoints (with a 1 mm spacing) using the 2-D Fourier transform method. From the standard deviation about the mean values, the random errors in horizontal and vertical displacement components were estimated as 0.2 and 1.1 μm, respectively.

CONCLUSIONS

A new technique for analysing the Young's fringe patterns from a double exposure speckle photograph has been proposed and evaluated. The method, based on maximum likelihood estimation, incorporates knowledge of the fringe noise statistics, and results in a substantial reduction in the random errors with no increase in systematic errors, compared to the 2-D Fourier transform method. The computation time is currently 30 times longer, but could be reduced by the use of a more specific maximization routine.

The technique of white light speckle photography for measuring wholefield, in-plane displacements and strains, has been successfully extended to include a scanning electron microscope as the means of imaging the speckle pattern. The increased resolution of the electron microscope over optical systems allows the use of a smaller speckle diameter, resulting in increased resolution, accuracy and sensitivity. Magnesium oxide crystals were found to provide a suitable speckle pattern with a speckle diameter of 0.5 μm, resulting in a spatial resolution of 15 μm and random errors of 16 nm.

High speed laser speckle photographs have been recorded using a rotating mirror camera. The randomly-spaced light pulses from a ruby laser can be controlled by repetitive Q-switching, and it has been shown how the resulting pulse trains may be synchronised with the frames of the camera. Double exposure photographs of a specimen undergoing rigid body displacement were found to produce good quality Young's fringes at interframe times down to 2 μs.

ACKNOWLEDGMENTS

J.M.H. is grateful to the Royal Society for a Research Fellowship. M.B.W. is supported by a CASE studentship from the Science and Engineering Research Council and Nuclear Electric plc; H.T.G. has a studentship from A.W.E., Aldermaston.

REFERENCES

1. Ennos, A.E. "Speckle interferometry" in *Laser Speckle and Related Phenomena*, Dainty, J.C. ed. Springer-Verlag, 1975.
2. Forno, C. "White light speckle photography for measuring deformation, strain and shape". Opt. Laser Tech., 7, 217-221, 1975.
3. Ineichen, B., Eglin, P. and Dandliker R. "Hybrid optical and electronic image processing for strain measurments by speckle photography". Appl. Opt., 19, 2191-2195, 1980.
4. Kaufmann, G.H., Ennos, A.E., Gale, B. and Pugh, D.J. "An electro-optical read-out system for analysis of speckle photographs". J. Phys. E., 13, 579-584, 1980.
5. Robinson, D.W. "Automatic fringe analysis with a computer image-processing system", Appl. Opt., 22, 2169-2176, 1983.
6. Meynart, R. "Instantaneous velocity field measurements in unsteady gas flow by speckle velocimetry". Appl. Opt., 22, 535-540, 1983.
7. Huntley, J.M. "An image processing system for the analysis of speckle photographs". J. Phys. E., 19, 43-48, 1986.
8. Huntley, J.M. "Speckle photography fringe analysis by the Walsh transform". Appl. Opt., 25, 382-386, 1986.
9. Huntley, J.M. "Speckle photography fringe analysis: assessment of current algorithms". Appl. Opt., 28, 4316-4322, 1989.
10. Goodman, J.W. "Statistical properties of laser speckle patterns" in *Laser Speckle and Related Phenomena*, Dainty, J.C. ed. Springer-Verlag, 1975.
11. Chiang, F.P. and Li, D.W. "Random (speckle) patterns for displacement and strain measurement: some recent advances," Opt. Eng., 24, 936-943, 1985.
12. Whitworth, M.B., Palmer, S.J.P., Huntley, J.M. and Field, J.E. "Speckle microphotography with the scanning electron microscope". Proc. Intl. Conf. Fringe Analysis, Loughborough, April 1989.
13. Pickering, C.J.D. and Halliwell, N.A. "Speckle photography in fluid flows: signal recovery with two-step processing". Appl. Opt., 23, 1128-1129, 1984.
14. Hu, X.M., Palmer, S.J.P. and Field, J.E. "The application of high-speed photography and white light speckle to the study of dynamic fracture". Opt. Laser Tech.,16, 303-306, 1984.
15. Rowlands, R.E., Taylor, C.E. and Daniel, I.M. "Ultra high-speed framing photography employing a multiply-pulsed ruby laser and a "smear-type" camera: application to dynamic photoelasticity". Proc. 8th Intl. Cong. High Speed Photography, Stockholm, 1968, 275-280.
16. Yamaguchi, I. "Fringe formation in speckle photography". J. Opt. Soc. Am. A, 1, 81-86, 1984.

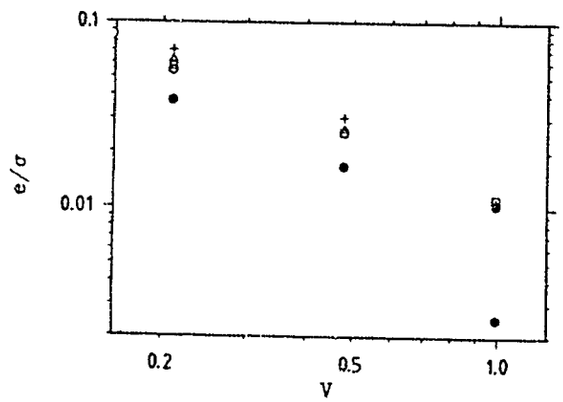

Fig. 1: Non-dimensional random error e/σ (random error = e; speckle diameter = σ), as a function of fringe visibility V, from five fringe analysis algorithms (1-D integration (Δ), 1-D autocorrelation (+), 2-D Fourier transform (o), 2-D Walsh transform (□), and maximum likelihood (•)).

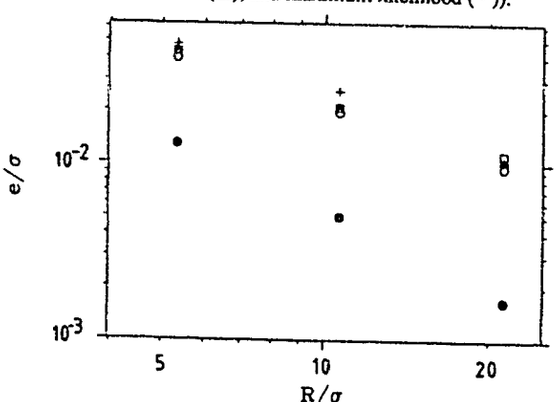

Fig. 2: Non-dimensional random error e/σ, as a function of non-dimensional laser probe radius R/σ, from five fringe analysis algorithms (symbols as in Fig. 1).

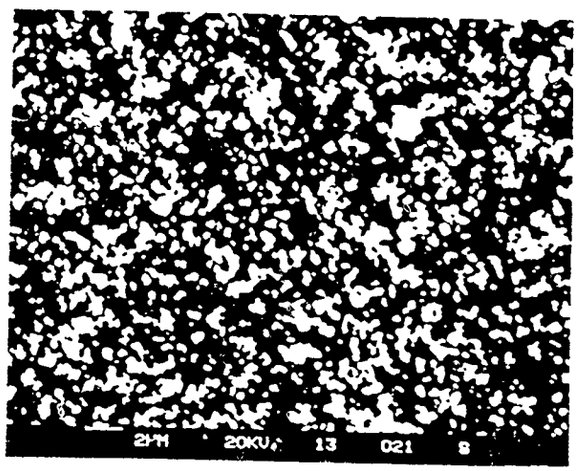

Fig. 3: Scanning electron micrograph of a speckle pattern of magnesium oxide crystals on the surface of polished aluminium. Field of view = 22 x 30 μm^2.Typical speckle diameter ≈ 0.5 μm.

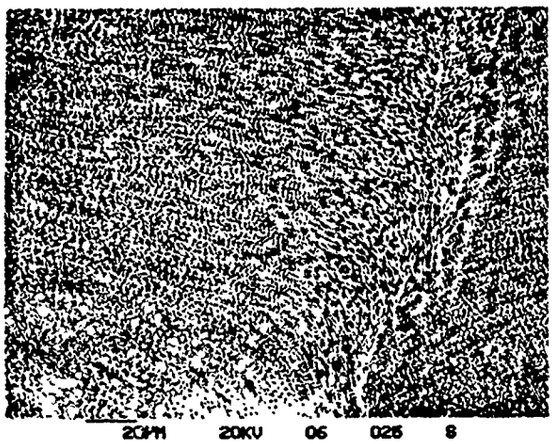

Fig. 4: Double exposure scanning electron micrograph of a speckle pattern on aluminium.Field of view = 160 x 220 μm^2.The specimen was strained between exposures, resulting in the surface microcrack towards the bottom right of the image. This photograph is a contact print of the original micrograph onto high contrast film (Ilford Technical line film).

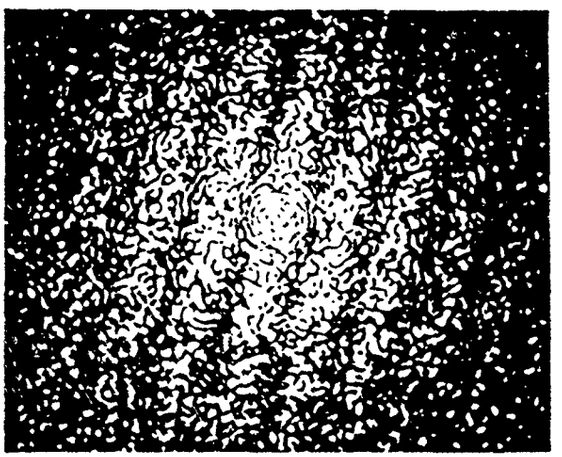

Fig. 5: Typical Young's fringe pattern, generated by probing the speckle micrograph of Fig. 4 with a laser beam of diameter 1.9 mm. Fringe visibility ≈ 40%.

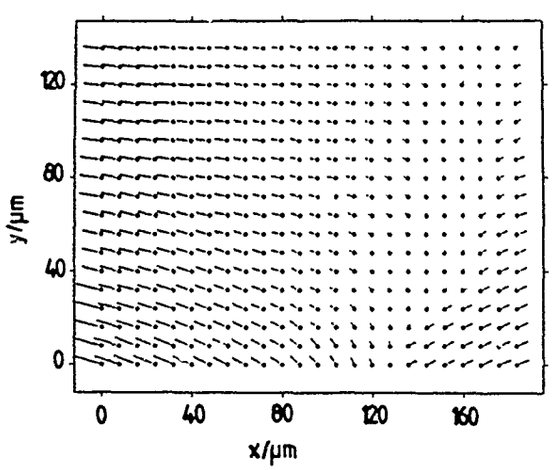

Fig. 6: Measured displacement field from Fig. 4. Material which was positioned at one of the dots at the first exposure had moved to the end of the line connected to the dot by the time of the second exposure. Displacements have been scaled by a factor of 2 relative to the coordinate system.

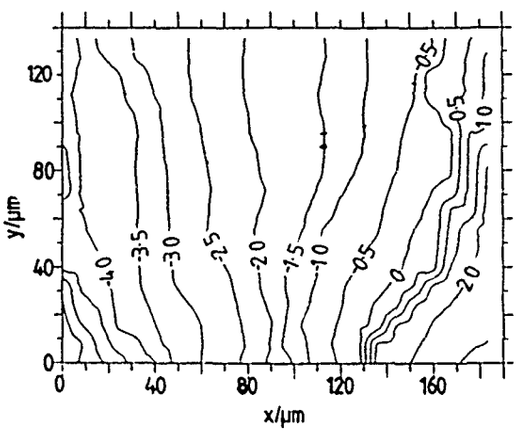

Fig. 7: Contour map of u_x / µm (horizontal displacement component) measured from Fig. 4. Contour interval = 0.5 µm.

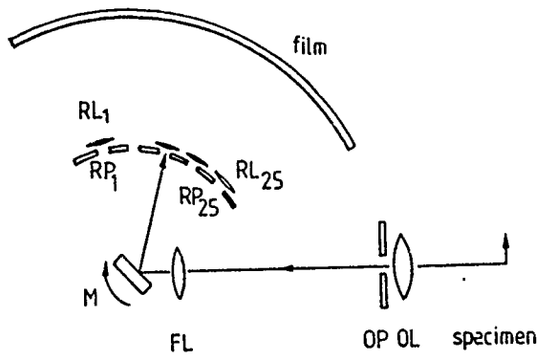

Fig. 8: Layout of the Beckman and Whitley rotating mirror camera used to record the dynamic speckle photographs. The notation used is explained in the text.

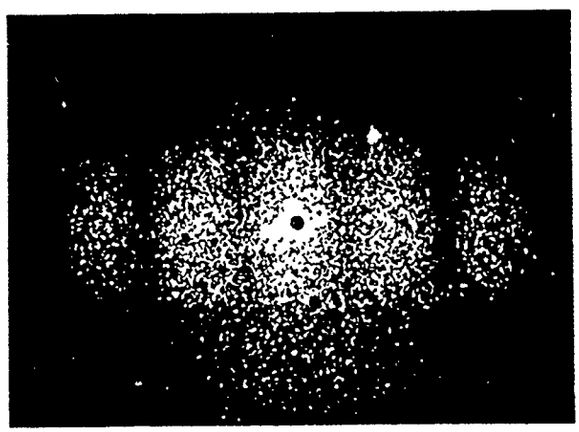

Fig 10: Young's fringe pattern from a double exposure laser speckle photograph recorded at 2 μs frame^{-1}.

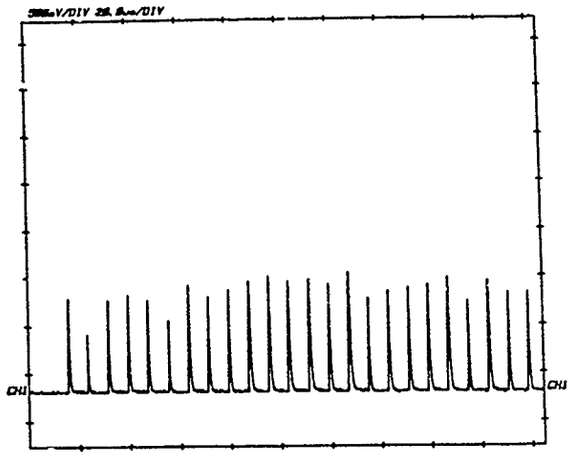

Fig. 9: Photodiode signal showing the light output from the ruby laser operating at an interframe time of 8 μs. Timebase = 20 μs div^{-1}.

APPENDIX 2

Proc. 19th intl. conf. on High Speed Photography and Photonics 1358 1:7
Cambridge, U.K. 16th - 21st Sept 1990

High speed photography of high resolution moiré patterns

M.B.Whitworth, J.M.Huntley and J.E.Field

University of Cambridge, Cavendish Laboratory
Madingley Road, Cambridge CB3 0HE, England

ABSTRACT

The techniques of high resolution moiré photography and high speed photography have been combined to allow measurement of the in-plane components of a transient displacement field with microsecond time resolution. Specimen gratings are prepared as casts in a thin layer of epoxy resin on the surface of a specimen. These are illuminated with a flash tube and imaged onto a reference grating with a specially modified camera lens, which incorporates a slotted mask in the aperture plane. For specimen gratings of 75 lines mm^{-1}, this selects the +1 and -1 order diffracted beams, thus doubling the effective grating frequency to 150 lines mm^{-1}. The resulting real-time moiré fringes are recorded with a Hadland 792 image converter camera (Imacon) at an inter-frame time of 2-5μs. The images are digitised and an automatic fringe analysis technique based on the 2-D Fourier transform method is used to extract the displacement information. The technique is illustrated by the results of an investigation into the transient deformation of composite disc specimens, impacted with rectangular metal sliders fired from a gas gun.

2. INTRODUCTION

High resolution moiré photography [1-3] is a development of the classical moiré grid method for measuring in-plane displacement. The main feature of the technique is that the specimen grating is imaged using a lens which has a mask placed in its aperture plane. The mask is designed to tune the lens to the spatial frequency of the specimen grating, resulting in images of high contrast and an improved depth of field. Burch and Forno used the technique to study quasi-static deformation of large engineering structures: double exposure photographs were recorded on a high resolution emulsion and subsequently spatially filtered. This approach is difficult to apply to dynamic problems, however, because of the limited spatial resolution of most high speed cameras. At the last congress on High Speed Photography and Photonics,[4] and in reference 5, Huntley and Field described a technique in which the specimen grating was imaged onto a reference grating, forming real-time moiré fringes. These have much lower spatial frequency components than the original gratings and can be resolved by a high speed camera. Gratings with 150 lines mm^{-1} were used, allowing displacement fields to be measured to an accuracy of ~1 μm, with microsecond time resolution.

In the present paper, we describe the further development of this technique. Reflective phase gratings have been applied to specimens, allowing the study of opaque materials. Additionally, the imaging system has been modified to make it telecentric on the object side. This eliminates errors due to out-of-plane movement of the specimen.

3. FORMATION OF FRINGES

The lens used to image the specimen grating onto the reference grating (Olympus 80mm f/4 macro) is shown in Fig. 1. The lens has been modified by inserting a slotted mask in the aperture plane, with a slot separation of 8.2 mm and slot width of 0.82 mm. The effect of the mask is to tune the optical transfer function of the lens to a narrow range of spatial frequencies.[1-3] When operating at a magnification of 1:1, and with a wavelength of ~490 nm, the tuned frequency is 150 lines mm^{-1} for the mask in Fig. 1.

Fig. 2 illustrates the use of the lens to record moiré fringes in reflection. X is a Xenon flash tube, which is imaged onto a slot, S, to provide a narrow light source, of dimensions comparable to one of the slots in OL_1. This light is reflected by a pellicle beam splitter, BS, to illuminate the specimen grating, SG through a field lens, FL_1. This has been added to collimate the light and render the system telecentric. OL_1, the masked objective, images the specimen grating SG onto the reference grating RG at a magnification of approximately 1:1. A second objective, OL_2, images RG onto the photocathode of a high speed camera.

In references 4 and 5, FL_1 was behind the (transparent) specimen and produced convergent illumination; in the present arrangement, it is placed in front of the specimen, resulting in a collimated beam incident on SG. This makes the system

telecentric on the object side. Previously, an out-of-plane displacement, u_z of the specimen would cause a change in magnification of SG, resulting in a fictitious uniform in-plane strain, $e_{fict} = u_z / 2f$, where f is the focal length of OL_1. For f = 80 mm, an out-of-plane displacement of 0.1mm would result in a fictitious strain of 0.6 millistrain. This corresponds to about one fringe order over a distance of 1cm. A telecentric system results in a magnification which is insensitive to motion of the specimen, thus eliminating this potential problem.

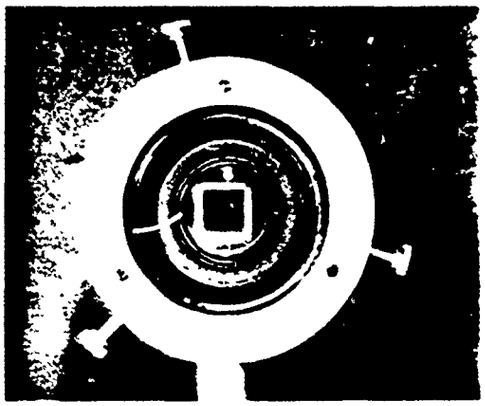

Fig. 1. The modified lens, showing the slotted mask in the aperture plane

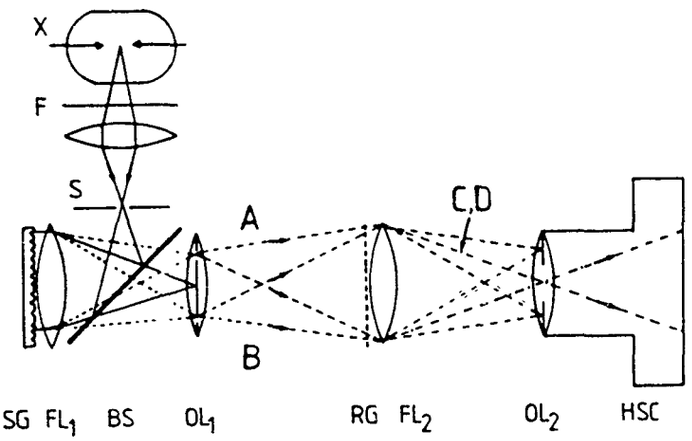

Fig. 2. The optical arrangement for the formation of moiré fringes in reflection

The pellicle beam splitter, BS, is a further extension to the optical system. This is necessary if the system is to operate in reflection, but has the disadvantage of causing 75% of available light to be lost. An attempt was made to image the light source onto a small fully silvered mirror placed between the slots of OL_1, but the distance betweer the front of OL_1 and its aperture is too large to avoid such a mirror casting a shadow across the slots. The problem of light loss has been partially alleviated by improving the diffraction efficiency of the gratings.

Huntley and Field [4,5] initially used 150 lines mm^{-1} gratings, but were able to improve the fringe contrast by halving the frequency of the reference grating and stopping down OL_2 to block the image of the mask, thus maintaining an effective grating frequency of 150 lines mm^{-1}. This process has now been taken a stage further by also halving the frequency of the specimen grating, and allowing the +1 and −1 order diffracted beams to pass through the mask in OL_1 while the 0 order beam is blocked. Fig. 2 illustrates a simple 1--D analysis of this situation. Consider a monochromatic point source within the slot S, which is imaged to the centre of OL_1. The wavelength, specimen grating pitch, and the spacing of the slots of OL_1 have been chosen such that the 1st order diffracted beams, A and B, pass through the slots. A and B then pass through RG and FL_2, but the direct beams are blocked by the iris diaphragm of OL_2 and only the 1st order diffracted beams are transmitted. The image is formed from the −1 diffracted beam from A and from the +1 diffracted beam from B (denoted C,D respectively).

The specimen and reference gratings are phase gratings and have aperture functions $f_s(y)$ and $f_r(y)$ which are assumed to take the form

$$f_s(y) = \frac{(1 + i\, d_s \cos 2\pi v_s y)}{2} \quad (1)$$

$$f_r(y) = \frac{(1 + i\, d_r \cos 2\pi v_r y)}{2} \quad (2)$$

where y is distance measured perpendicular to the grating lines, d_s, d_r are proportional to the first-order amplitude diffraction efficiencies ($0 \le d_s, d_r \le 1$), and v_s, v_r are the spatial frequencies of the specimen and reference gratings, respectively. If it is assumed that the lenses are thin and free of aberrations, the amplitude distribution of beams A and B in the plane of RG, can be written as

$$a_A(y) = i\, d_s\, g(y) \exp(2\pi i\, v_s\, y) \quad (3)$$

$$a_B(y) = i\, d_s\, g(y) \exp(-2\pi i\, v_s\, y) \quad (4)$$

where g(y) is a complex function, with a modulus of unity, to allow for the fact that the light is not collimated in the plane of RG.

The amplitude distributions of beams C and D in the film / photocathode plane of the camera, are given by

$$a_C(y) = -\, d_s\, d_r\, g(y) \exp(2\pi i\, [v_s - v_r]\, y) \quad (5)$$

$$a_D(y) = -\, d_s\, d_r\, g(y) \exp(2\pi i\, [v_r - v_s]\, y) \quad (6)$$

The intensity distribution in the film plane is given by

$$I(y) = |a_C + a_D|^2$$

$$= 2\, d_r^2\, d_s^2 \{1 + \cos(2\pi\, 2[v_r - v_s]\, y)\} \quad (7)$$

It can be seen from this that the effective frequencies of both gratings have been doubled and that the exclusion of the direct beam from SG has resulted in a contrast which is independent of diffraction efficiency. Thus it should be possible to work with gratings of poor diffraction efficiency, although the brightness of the fringes will be reduced.

Prior to the recording of a photographic sequence, the position of OL_1 is adjusted to produce linear mismatch fringes. These fringes are equivalent to an initial fictitious strain, either compressive or tensile depending on whether SG is imaged onto RG at a magnification of less than or greater than unity. The mismatch fringes act as carrier fringes, which are needed for application of the automatic fringe analysis technique described later.

4. PREPARATION OF GRATINGS

The specimen and reference gratings were created by forming a two beam interference pattern from a HeNe laser and recording this on a glass plate (Agfa 10E75 emulsion). Gratings prepared in this way are suitable for use in transmission as reference gratings, although an improvement in diffraction efficiency is obtained by bleaching the holographic plate, thus forming a phase grating. Huntley and Field [4,5] prepared specimen gratings for use in transmission by applying an amplitude grating recorded on polyester film, to the surface of the specimen. For gratings operating in reflection, phase gratings are cast in a layer of epoxy resin or of silicone rubber on the surface [6] in the following way:

A grating is formed on a holographic plate, which is developed and then washed in a solution of wetting agent. The grating is then aluminised by vacuum deposition. A small quantity of epoxy resin is applied to the grating and the specimen is placed on top, spreading the epoxy out into a thin layer. When the resin has cured, the grating is separated from the specimen, leaving an aluminised cast of the grating on the surface of the specimen. The diffraction efficiency of these gratings is better than that of the amplitude gratings used in references 4 and 5.

With the telecentric imaging system, field lens FL_1 introduces distortion which makes it difficult to achieve parallel carrier fringes. This effect can be eliminated by the use of a compensated reference grating, prepared in-situ. A two beam interference pattern is formed in the plane of the specimen grating (which is not present at this stage). This is imaged into the reference grating plane by FL_1 and OL_1 with the masked aperture removed. The resulting diffraction pattern is recorded on a holographic plate and used as the reference grating.

5. SLIDER IMPACT OF COMPOSITE DISCS

In this experiment, disc specimens were impacted by rectangular projectiles made of phosphor bronze. The discs are 5mm thick and consist of a central polycarbonate region with a diameter of 15.9 mm, 19.1 mm, or 22.2 mm, surrounded by a copper ring of external diameter 25.4 mm and wall thickness 1.6 mm. The intervening region is filled with silicone rubber. Diffraction gratings were applied to the polycarbonate region. The purpose of the experiment was to measure the level of strains that are present in the polycarbonate region for varying thicknesses of rubber, using the reflection moiré technique illustrated in Fig. 2.

The projectiles are fired by means of a rectangular bore gas gun with a double diaphragm valve [7,8]. This was arranged to give projectile velocities of 56.0 ± 1.1 m s^{-1}. Triggering of the flash and camera was achieved by the projectile breaking a laser beam and the impact velocity was calculated from a time of flight measurement over a length of 25 mm. In order to protect the field lens FL_1 from damage, a 1 mm thick sheet of polycarbonate was placed between the lens and the specimen.

Fig. 3 shows a high speed sequence of a disc specimen undergoing impact. Only the central polycarbonate region is visible, this having a diameter of 19.1 mm. The gratings were vertical, so the fringes represent the horizontal displacement component, and compressive strains show up as a decrease in fringe spacing. The interframe time is 5 μs. A compressive stress wave can be seen entering the polycarbonate from the left, crossing the disc in approximately 15 μs. This reflects from the right hand surface as a tensile wave, cancelling the effect of the incident wave as can be seen in frame 3.

6. ANALYSIS OF FRINGE PATTERNS

The use of high speed photography has resulted in the generation of a large number of moiré fringe patterns, the manual analysis of which is very time consuming (one 7 frame sequence took 50 man hours). For this reason, an automatic analysis system has been developed [4,5].

The fringe patterns are obtained from the Imacon as negative images on Kodak T-Max 400 film, push processed to 3200 ASA. These are digitised to a resolution of 256 x 256 pixels by projecting them onto a photodiode array. Analysis is based on a 2-D Fourier transform method.[5] The fringe pattern is first windowed to isolate the area of the specimen from the background. The d.c. intensity level of the pattern is subtracted, and a 2-D Fourier transform is then performed. The carrier fringes result in two main peaks and a central peak which is a remnant of the d.c. term. A window is applied to select one of these peaks, the remainder of the transform plane being set to zero; this is followed by an inverse Fourier transform. The image is now a complex 2-D array, where the phase at any point equals the phase of the original fringes, but wrapped onto the range 0 to 2π. The phases are unwrapped onto a continuous range by means of a noise immune phase unwrapping algorithm.[9] Each 2π phase change represents a change in displacement equal to the grating pitch, and so a scaling of the phase map results in a displacement map. This map is the sum of a fictitious displacement resulting from the mismatch fringes, and the displacement due to impact. The fictitious displacement field can be determined and removed by analysing a sequence of photographs recorded before the event with no deformation present. Thus analysis of an event lasting for eight frames involves application of the Fourier transform method to 16 images. Once the appropriate filter has been established by examining the Fourier transform of one of the images, all 16 are processed automatically by the computer. Fig. 4 shows the results from the analysis of the eight frames of Fig. 3. The contour interval is 2μm.

7. CONCLUSION

At the last congress on High Speed Photography and Photonics, Huntley and Field [4] demonstrated the feasibility of using a high speed camera to record high resolution moiré fringes. We have now developed that system to work in reflection, increasing the range of applicability to include opaque specimens. The loss of light incurred by use of a beam splitter has been compensated for by the improved diffraction efficiency gained through the use of phase gratings. Additionally the system has been altered to double the frequency of both gratings, resulting in a fringe contrast which is independent of the diffraction efficiencies of the gratings. A final modification has been to make the system telecentric, with the effect of

eliminating fictitious strains resulting from out of plane motion of the specimen. The new system has been used to make whole field measurements of the displacements occuring when a composite disc specimen is impacted by a metal slider.The effective grating frequency of 150 lines mm^{-1} is substantially higher than conventional moiré photography, giving a basic sensitivity of 6.7 μm / fringe. An automatic fringe analysis technique based on the 2-D Fourier transform method has been used to determine displacement fields to an accuracy of the order of 1 μm.

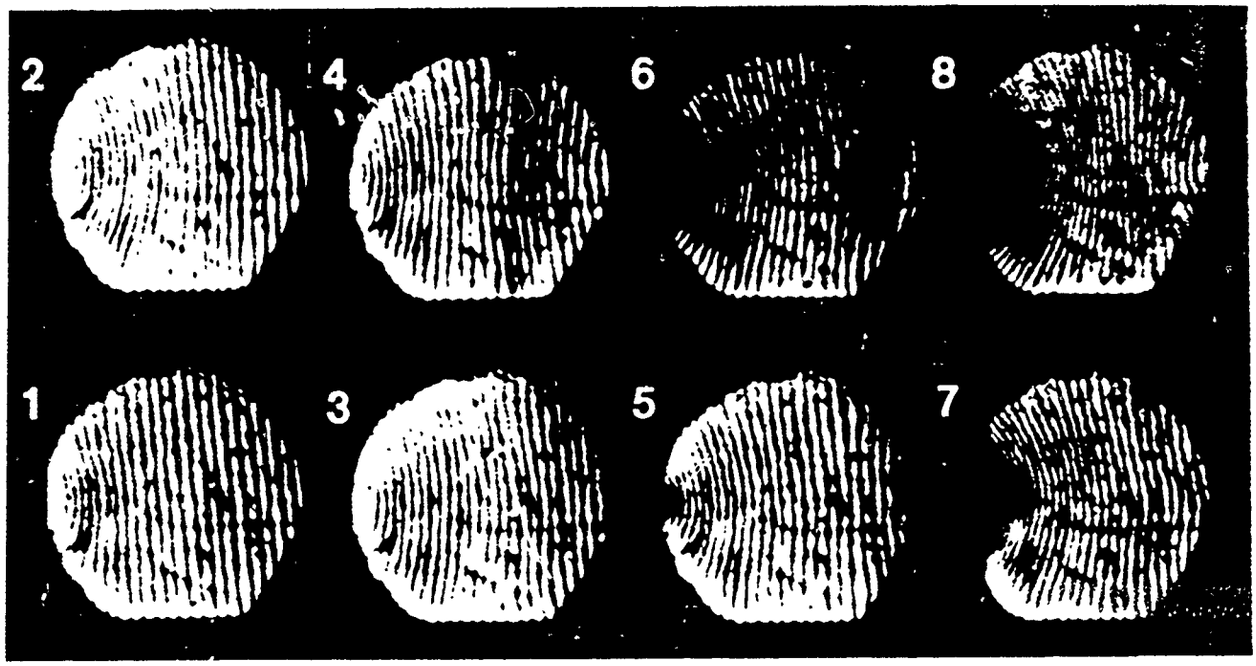

Fig. 3. A high speed moiré sequence of the central region of a composite disc undergoing impact by a slider

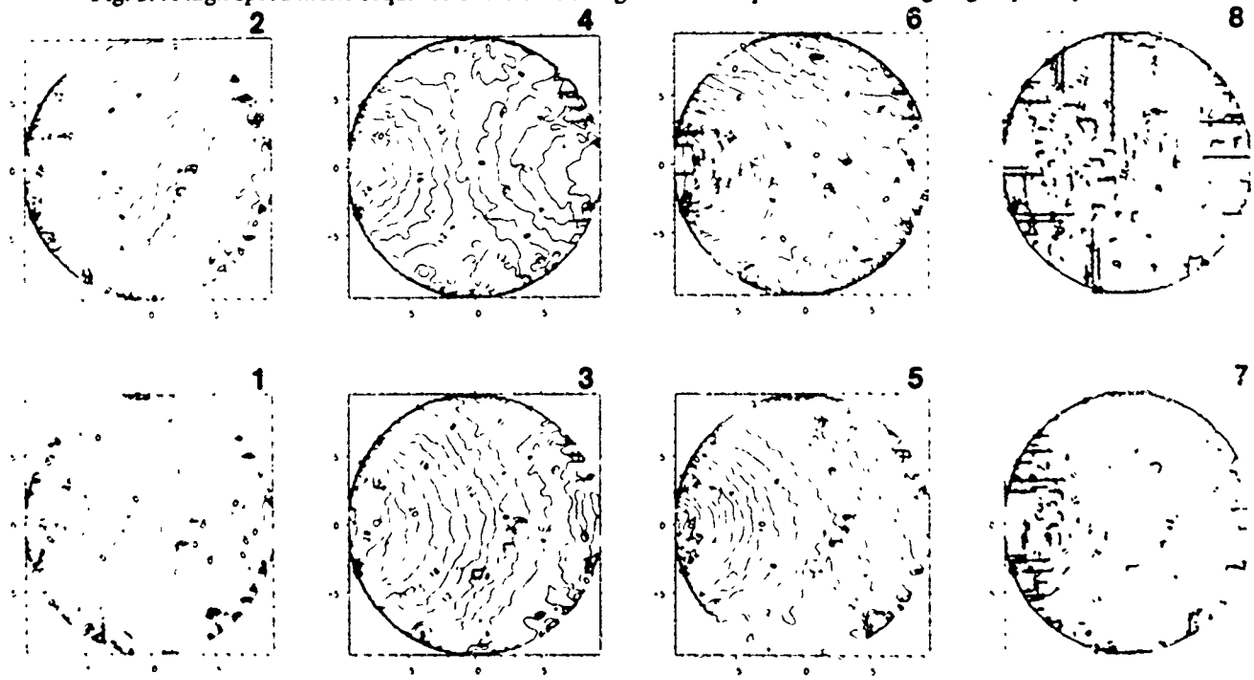

Fig. 4. Contours of the horizontal displacement component for the high speed sequence of Fig. 3

8. ACKNOWLEDGEMENTS

M.B.W. was supported by a CASE studentship from the Science and Engineering Research Council, and Nuclear Electric plc. J.M.H. acknowledges support in the form of a Royal Society Research Fellowship.

9. REFERENCES

1 J.M. Burch and C. Forno, "High sensitivity moiré grid technique for studying deformation in large objects," *Opt. Eng.* 14(2) pp. 178-185, 1975.
2 J.M. Burch and C. Forno, "High resolution moiré photography," *Opt. Eng.* 21(4) pp. 602-614, 1982.
3 C. Forno, "Deformation Measurement using high resolution moiré photography," *Opt. Lasers Eng.* 8 pp. 189-212, 1988.
4 J.M. Huntley and J.E. Field, "Application of laser speckle and moiré photography to the study of dynamic fracture," *Proc. SPIE* 1032 pp. 1012-1021, 1988
5 J.M. Huntley and J.E. Field, "High resolution moiré photography: application to dynamic stress analysis," *Opt. Eng.* 28(8) pp. 926-933, 1989.
6 D. Post, "Moiré Interferometry," Handbook on Experimental Mechanics A.S. Kobayashi pp. 314-387 Prentice-Hall, Englewood Cliffs, 1987.
7 I.M. Hutchings, M.C. Rochester and J-J. Camus, "A rectangular bore gas gun," *J. Phys. E* 10 pp. 455-457, 1977.
8 I.M. Hutchings, "The erosion of ductile metals," Ph.D. thesis, University of Cambridge, 1974.
9 J.M. Huntley, "Noise-immune phase unwrapping algorithm," *Appl. Opt.* 28(15) pp. 3268-3270, 1989.